A first order hyperbolic reformulation of the Navier-Stokes-Korteweg system based on the GPR model and an augmented Lagrangian approach

Firas Dhaouadi*[a], Michael Dumbser[a]

[a]*Department of Civil, Environmental and Mechanical Engineering, University of Trento, Via Mesiano 77, 38123 Trento, Italy.*

Abstract

In this paper we present a novel first order hyperbolic reformulation of the barotropic Navier-Stokes-Korteweg system. The new formulation is based on a combination of the first order hyperbolic Godunov-Peshkov-Romenski (GPR) model of continuum mechanics with an augmented Lagrangian approach that allows to rewrite nonlinear dispersive systems in first order hyperbolic form at the aid of new evolution variables. The governing equations for the new evolution variables introduced by the rewriting of the dispersive part are endowed with curl involutions that need to be taken care of. In this paper, we account for the curl involutions at the aid of a thermodynamically compatible generalized Lagrangian multiplier (GLM) approach, similar to the GLM divergence cleaning introduced by Munz *et al.* for the divergence constraint of the magnetic field in the Maxwell and MHD equations. A key feature of the new mathematical model presented in this paper is its ability to restore hyperbolicity even for non-convex equations of state, such as the van der Waals equation of state, thanks to the use of an augmented Lagrangian approach and the resulting inclusion of surface tension terms into the hyperbolic flux.

The governing PDE system proposed in this paper is solved at the aid of a high order ADER discontinuous Galerkin finite element scheme with *a posteriori* subcell finite volume limiter in order to deal with shock waves, discontinuities and steep gradients in the numerical solution. We propose an exact solution of our new mathematical model, show numerical convergence rates of up to sixth order of accuracy and show numerical results for several standard benchmark problems, including travelling wave solutions, stationary bubbles and Ostwald ripening in one and two space dimensions.

Keywords: first order hyperbolic reformulation of nonlinear dispersive systems, augmented Lagrangian approach, thermodynamically compatible generalized Lagrangian multiplier (GLM) curl cleaning, ADER Discontinuous Galerkin schemes with *a posteriori* subcell finite volume limiter, unified first order hyperbolic formulation of continuum mechanics, compressible multi-phase flows,

1. Introduction

Generally in mechanics, most of the prominent models stem from a local description of the continuum, *i.e* the medium is taken as a set of infinitesimal elements, each of which can be considered independent, but can still interact with their closest neighbors when the exchange of conserved quantities is at stake [60]. In such a setting, the deformation of the medium can be fully determined by constitutive laws that only depend on the first gradient of the displacement field. While this approach is often satisfactory, it fails to provide an accurate description of the motion in some cases, out of which we single out dispersive phenomena, and more particularly compressible fluid flows with surface tension.

*Corresponding author

Email addresses: firas.dhaouadi@unitn.it (Firas Dhaouadi*), michael.dumbser@unitn.it (Michael Dumbser)

Effects of surface tension usually manifest in multi-phase flows, where one or more interfaces divide the fluid into separate regions with different thermodynamic properties. While it is acknowledged that interfaces are sustained by capillary forces, there are different theories that argue their true physical nature. A complete examination of these theories and their history is not in the scope of this work. Nevertheless, it seems of importance to recall some of the contributions that set the theoretical foundation for our model. The reader is referred to [71] for a thorough review of the history.

The first attempts to describe the mechanics of the interface date back to Young, Laplace and Maxwell in the 19th century. In their formalism, every phase is considered as an independent fluid and one needs to take into account suitable compatibility conditions on the interface. An alternative theory was forwarded by Van der Waals in 1893 [78], after Maxwell's contribution to the matter. In contrast to its predecessors, Van der Waals proposed a continuous transition of the fluid density across a finite-length layer between the liquid and its vapor and stated that equilibria where the density distribution is heterogeneous, are compatible with capillarity, only if the free energy at a point, not only depended on its local density, but also on the densities in the neighboring points [78, 61]. Based on the work of Van der Waals, Korteweg formulated a constitutive equation of the Cauchy stress that is a function of both density and its spatial gradients in the static case [62]. From the continuum mechanics' standpoint, the deformation in this case also depends on the second gradient of the displacement field, earning this theory the well-known name of *second gradient theory*. The dynamical form of the equations, based on Hamilton's principle of stationary action, was obtained by Casal [25, 26] and a year later independently by Eglit [53]. In the absence of dissipation, these equations came to be known as the Euler-Korteweg system. Its applications extend beyond the scope of capillary fluids to also reach quantum hydrodynamics and thin films flows, and have been the subject of extensive studies in the recent decades [6, 8, 9, 10, 16, 17, 15, 27, 56, 58, 66, 3].

Navier-Stokes-Korteweg (NSK) equations can be seen as a dissipative regularization of the Euler-Korteweg system, obtained by adding viscous stresses to the latter. It is widely used to model viscous two-phase flows when supplemented with specific non-convex equations of state of the Van der Waals type. In the frame of the NSK equations, the fluid is considered to be a single phase where the bulk fluids are distinguished only through the value of density. Thus, the same mono-phase system of equations describes the fluid motion in the entire domain. In the context of numerical simulations of compressible multi-phase flows, there are both benefits and drawbacks when addressing this system of equations. First, there is no need to explicitly track the interface position, since the latter per se does not exist but is rather smeared out. This makes the so-called *diffuse interface* approach more suitable to address problems where strong topological changes in the interface occur, such as droplet breakup or coalescence. Besides, in the vicinity of the critical temperature, an interface is no longer discernible, making it unclear how to tackle the problem using a sharp interface approach. On the other hand, discretizing the NSK equations by classical finite-volumes and finite differences is conditioned by severe time-stepping constraints due to the high-order derivatives present in the equations, especially when considering multi-dimensional computations. An additional difficulty comes from the associated Van der Waals equation of state, which admits a region of non-convexity, inside of which the Euler subsystem loses hyperbolicity, rendering the use of classical Godunov-type finite volume based methods very difficult, or even impossible. For a high order local discontinuous Galerkin finite element method applied directly to the original NSK model, see the interesting work of Diehl *et al.* [37]. In recent advances, relaxation methods were adopted to deal with the above mentioned difficulties. In particular a parabolic relaxation approach was introduced by Rohde in [69] and developed further in subsequent works [32, 65, 29, 59]. The approach allows to approximate the NSK system by a second-order system of mixed hyperbolic-parabolic type, allowing for a more flexible choice of numerical methods.

The main purpose of this paper is to provide a new *first order hyperbolic* reformulation of the Navier-Stokes-Korteweg equations, combining the first order hyperbolic Godunov-Peshkov-Romenski (GPR) model of continuum mechanics [70, 68, 48] with the hyperbolic Euler-Korteweg equations of [35] that make use of an extended Lagrangian approach forwarded in [55]. We emphasize that the hyperbolic model proposed in this paper remains hyperbolic even for non-convex equations of state if a sufficiently stiff (small) penalty

parameter is used in the augmented Lagrangian setting.

In order to deal with the curl constraints present in the equations, we make use of a thermodynamically compatible GLM curl cleaning technique, following the ideas forwarded in [46, 30, 20] and which extend the classical hyperbolic GLM divergence cleaning introduced by Munz *et al.* in [64, 34] for the Maxwell and MHD equations to the case of hyperbolic PDE systems with curl involutions.

This paper is organized as follows. Section 2 presents a brief recall of the Navier-Stokes-Korteweg equations and the Van-der-Waals equation of state, followed by a description of the equations of our model. We present an eigenstructure analysis in order show that the model is hyperbolic in one and two dimensions of space. A comparison of the dispersion relation properties is finally provided and compared with those of the original Navier-Stokes-Korteweg system. In Section 3, we present the details of the ADER-DG scheme with *a posteriori* subcell finite volume limiter that is used for the numerical simulations. Numerical results in one and two dimensions, in the stationary and non-stationary case are presented thereafter in Section 4. The paper closes with some conclusions and an outlook to future work in Section 5.

2. Mathematical model

2.1. The Navier-Stokes-Korteweg equations

The barotropic isothermal Navier-Stokes-Korteweg system is given by

$$\frac{\partial \rho}{\partial t} + \frac{\partial (\rho u_k)}{\partial x_k} = 0, \tag{1a}$$

$$\frac{\partial \rho u_i}{\partial t} + \frac{\partial \left(\rho u_i u_k + P\delta_{ik} - \sigma_{ik} - \kappa_{ik}\right)}{\partial x_k} = 0. \tag{1b}$$

In these equations and in the rest of this paper, $\mathbf{x} = [x_i] \in \mathbb{R}^d$ refers to the vector of space coordinates and $t \in \mathbb{R}_+$ represents time; $\rho = \rho(\mathbf{x}, t)$ is the fluid density and $\mathbf{u} = [u_i(\mathbf{x}, t)]$ is the velocity. The quantity $P = \rho W'(\rho) - W(\rho)$ represents the hydrostatic pressure, where $W(\rho)$ is the Helmholtz free energy, δ_{ik} is the Kronecker symbol denoting the $d \times d$ identity matrix, $\boldsymbol{\sigma} = [\sigma_{ij}]$ is the viscous stress tensor, and $\boldsymbol{\kappa} = [\kappa_{ij}]$ is the so-called Korteweg stress tensor, whose expressions are recalled below

$$\boldsymbol{\sigma} = \mu\left(\nabla\mathbf{u} + \nabla\mathbf{u}^T - \frac{2}{3}(\nabla\cdot\mathbf{u})\mathbf{I}\right), \quad \boldsymbol{\kappa} = \gamma\left(\frac{1}{2}|\nabla\rho|^2 + \rho\Delta\rho\right)\mathbf{I} - \gamma\nabla\rho\otimes\nabla\rho. \tag{2}$$

Here, μ is the dynamic viscosity and γ is the surface tension coefficient. The viscous stresses are expressed under the Stokes hypothesis. The dissipationless part of this system (*i.e* for $\mu = 0$), is the Euler-Korteweg system of equations with constant capillarity coefficient. It corresponds to the Euler-Lagrange equations of the following Lagrangian

$$\mathcal{L} = \int_{\Omega_t} \left(\frac{\rho}{2}|\mathbf{u}|^2 - W(\rho) - \frac{\gamma}{2}|\nabla\rho|^2\right) d\Omega, \tag{3}$$

obtained by virtue of a least action principle, under the total mass conservation constraint

$$\frac{\partial \rho}{\partial t} + \frac{\partial (\rho u_k)}{\partial x_k} = 0. \tag{4}$$

The total energy density can be expressed as follows

$$E = \frac{\rho}{2}|\mathbf{u}|^2 + W(\rho) + \frac{\gamma}{2}|\nabla\rho|^2, \tag{5}$$

where $\frac{\rho}{2}|\mathbf{u}|^2$ is the kinetic energy and $\frac{\gamma}{2}|\nabla\rho|^2$ is the surface tension term as in the gradient theory of Van der Waals. In the context of the sought applications *i.e* isothermal two-phase flows, see also [57, 63, 72], the

Helmholtz free energy must be such that a different equilibrium state for each phase exists, suggesting at least two local minima for the function $W(\rho)$, separated by a region that is non-convex in ρ. A standard choice fulfilling these assumptions and which we will consider throughout this paper is a Van der Waals equation of state, for which the pressure P and the double-well potential W are respectively given by

$$P(\rho) = \frac{\rho RT}{1-b\rho} - a\rho^2, \quad W(\rho) = \rho RT c_v(1 - \log(T)) + \rho RT \log\left(\frac{\rho}{1-b\rho}\right) - a\rho^2 \tag{6}$$

and are both represented in Figure 1 below. Throughout this paper, the parameters a, b, R and T will always have the following values:

$$a = 3, \quad b = \frac{1}{3}, \quad R = \frac{8}{3}, \quad T = 0.85, \quad c_v = \frac{3}{2}. \tag{7}$$

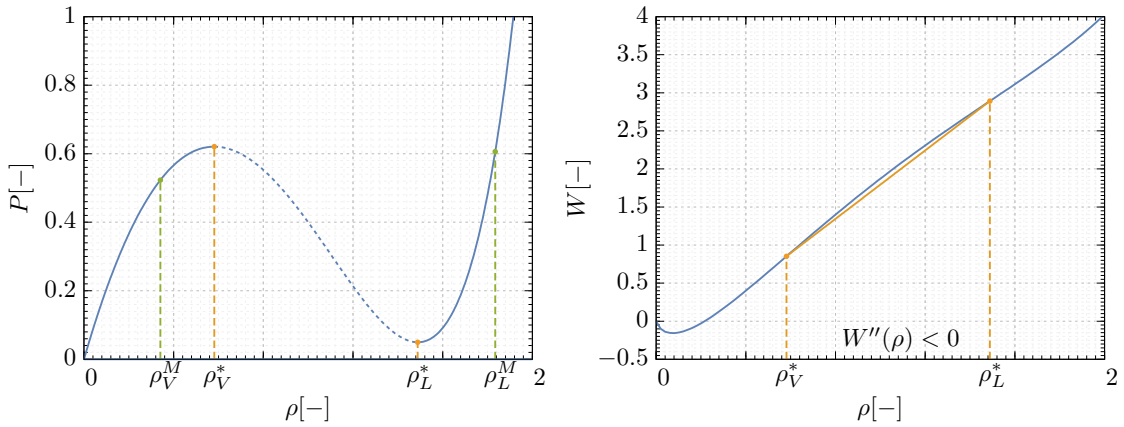

Figure 1: Pressure (left) and free energy (right) as functions of the density ρ for the values (7). ρ_V^M and ρ_L^M represent the Maxwell states for the vapor and liquid phase respectively. The pressure law has two extrema attained in ρ_V^* and ρ_L^* and which delimit the non-convex region of $W(\rho)$.

In the setting of the gradient theory of Van der Waals, in order for the fluid phases to coexist simultaneously as bulk phases, an additional force is needed to balance pressure in the density transitions. In this model, this is ensured by the surface energy term, where the coefficient γ acts as a penalty factor for gradients of density. Smaller values of γ allow for sharper transitions between the phase bulks. The limit $\gamma \to 0$ would then correspond to a sharp interface limit.

2.2. A hyperbolic relaxation to the Navier-Stokes-Korteweg system

In order to provide a new first-order hyperbolic model that approximates the barotropic Navier-Stokes-Korteweg equations (1), it is clear that substantial reformulations of both diffusive and dispersive processes are required, since the stress tensors $\boldsymbol{\sigma}$ and $\mathbf{K}$ contain terms that depend on high-order space derivatives. These terms are a source of concern not only from the computational point of view, but also from the mathematical point of view, given that the structure of the stress tensors, in their classical formulation, is incompatible with the framework of hyperbolic equations. In fact, while the latter is based on a bounded wave-speed formulation, the former diffusion and dispersive operators are known to exhibit infinite propagation speeds. An additional difficulty resides in the fact that the associated Van der Waals equation of state has a non-convex region, resulting in the loss of hyperbolicity in the left-hand side of system (1). Characteristics-based numerical methods for the Euler subsystem fail in this case as they generally rely on real-valued wave speeds.

The relaxation model we propose here, is founded on two key elements. The first ingredient is the Godunov-Peshkov-Romenski model of continuum mechanics [70, 68, 48]. The model provides an interesting formulation of the continuum, in which a so-called distortion field $\mathbf{A}(\mathbf{x}, t) = A_{ij}$, is used to describe the deformation of the material elements. It will be referred to as the distortion matrix throughout this paper. The time evolution of $\mathbf{A}$, when supplied with an appropriate stiff relaxation source term, allows to generalize the model beyond the scope of solid mechanics to include, inter alia, viscous and non-viscous fluid flows, with Newtonian or non-Newtonian rheologies, from which, the Navier-Stokes equations can be asymptotically recovered [48]. The second prerequisite key element is the so-called augmented Lagrangian formalism [35] which casts second-gradient dispersive systems into first-order hyperbolic equations, that are derived from variational principles. The merging of both theories, allows us to write a new first-order system approximating the Navier-Stokes-Korteweg equations and which is given as follows

$$\frac{\partial \rho}{\partial t} + \frac{\partial (\rho u_k)}{\partial x_k} = 0, \tag{8a}$$

$$\frac{\partial (\rho u_i)}{\partial t} + \frac{\partial \left(\rho u_i u_k + P\delta_{ik} - \Sigma_{ik} - K_{ik}\right)}{\partial x_k} = 0 \tag{8b}$$

$$\frac{\partial A_{ik}}{\partial t} + \frac{\partial A_{im} u_m}{\partial x_k} + u_j \left(\frac{\partial A_{ik}}{\partial x_j} - \frac{\partial A_{ij}}{\partial x_k} \right) = -S_{ik}, \tag{8c}$$

$$\frac{\partial (\rho \eta)}{\partial t} + \frac{\partial (\rho \eta u_k)}{\partial x_k} = \rho w, \tag{8d}$$

$$\frac{\partial p_i}{\partial t} + \frac{\partial (p_j u_j - w)}{\partial x_i} + u_j \left(\frac{\partial p_i}{\partial x_j} - \frac{\partial p_j}{\partial x_i} \right) = 0, \tag{8e}$$

$$\frac{\partial (\rho w)}{\partial t} + \frac{\partial \left(\rho w u_k - \gamma p_k/\beta\right)}{\partial x_k} = \frac{1}{\alpha\beta}\left(1 - \frac{\eta}{\rho}\right), \tag{8f}$$

The model consists of a total mass conservation equation (8a) for the density ρ, a conservation equation for the momentum $\rho\mathbf{u}$ (8b), in which the hydrostatic pressure is kept the same as in (1), and alternative stress tensors $\mathbf{K} = [K_{ij}]$ and $\mathbf{\Sigma} = [\Sigma_{ij}]$, appear in the momentum flux, representing the dispersive and viscous effects respectively. Their expressions are given by

$$\mathbf{K} = \left(\frac{\gamma}{2}|\mathbf{p}|^2 - \frac{\eta}{\alpha}\left(1 - \frac{\eta}{\rho}\right) \right) \mathbf{I} - \gamma \mathbf{p} \otimes \mathbf{p}, \qquad \mathbf{\Sigma} = -\rho c_s^2 \mathbf{G}\mathrm{dev}\mathbf{G}, \tag{9}$$

where $\mathbf{G} = \mathbf{A}^T\mathbf{A}$ is called the metric tensor. Equation (8c) is the time-evolution of the distortion matrix $\mathbf{A}$. The source term $\mathbf{S} = [S_{ik}]$ is defined by

$$\mathbf{S} = -\frac{3}{\tau}\det(\mathbf{A})^{5/3}\mathbf{A}\mathrm{dev}(\mathbf{G}), \tag{10}$$

where τ is the strain dissipation time. Equations (8d) to (8f) are auxiliary equations that come from the augmented Lagrangian method for the dispersive part of the Navier-Stokes-Korteweg system [35]. In these equations, η is a new degree of freedom that substitutes ρ as the new order parameter differentiating the bulk fluids. The variables $w = \dot{\eta} = \partial_t \eta + \mathbf{u} \cdot \nabla\eta$ and $\mathbf{p} = \nabla\eta$ are defined as the material derivative and the gradient of η respectively. The evolution equations (8d) and (8e) are thus obtained as a straightforward consequence of these definitions [35]. The non-conservative product that appears in equation (8e) is theoretically zero, given that $\mathbf{p}$ is a gradient field, thus curl-free by construction. This term must be maintained nonetheless for structure purposes and in particular to keep hyperbolicity in the multidimensional case. Finally, (8f) is an Euler-Lagrange equation obtained through a least-action principle applied to the system's Lagrangian

$$\mathcal{L} = \int_{\Omega_t} \left(\frac{\rho}{2}|\mathbf{u}|^2 - W(\rho) - \frac{\rho}{4}c_s^2 \mathrm{dev}\mathbf{G} : \mathrm{dev}\mathbf{G} - \frac{\gamma}{2}|\mathbf{p}|^2 + \frac{1}{2\alpha\rho}(\eta - \rho)^2 + \frac{\beta}{2}\rho w^2 \right) d\Omega, \tag{11}$$

with respect to η and its derivatives. Similarly, equation (8b) is also an Euler-Lagrange equation to the Lagrangian (11), with respect to the continuum variables that are ρ, $\mathbf{u}$ and $\mathbf{A}$. It seems necessary at this point to highlight that even though our model depends explicitly on the surface tension coefficient γ, the viscosity μ does not appear anywhere in the equations. Indeed, the constitutive part of the GPR model does not require explicit specification of the viscosity coefficient. However, in the fluid limit ($\tau \to 0$) the effective viscosity of the model can be computed via a Chapman-Enskog expansion [48] and it is equal to $\mu = \tau\rho_0 c_s^2/6$. Therefore, whenever we will need to simulate a fluid of a certain viscosity, we shall make use of this formula for the effective viscosity of the GPR model and impose τ and c_s accordingly. Moreover, it is also possible to asymptotically recover the original Korteweg stress tensor by replacing the term $\frac{\eta}{\alpha}(1-\frac{\eta}{\rho})$ which appears in the tensor $\mathbf{K}$ accordingly to equation (8f) and expanding in α and β [36].

By virtue of its definition, the vector $\mathbf{p}$ admits a curl involution constraint, that is $\nabla \times \mathbf{p} = 0$. While theoretically, this constraint is satisfied for all times if it is verified for $t = 0$, this is not guaranteed at the numerical level due to the buildup of round-off errors. In order to address this problem at the numerical level, we will use a thermodynamically compatible Generalized Lagrangian multiplier curl-cleaning technique [46, 30, 20], in the same fashion as in [20], where an additional field variable $\boldsymbol{\psi}$ is used as a means to propagate curl errors with a prescribed parameter b_c, with the purpose of avoiding their accumulation locally, which could lead to the failure of the numerical simulation [30]. In the setting of this method, an additional evolution equation is added for the so-called *cleaning field* $\boldsymbol{\psi}$, and which is coupled with the evolution equation for the gradient field $\mathbf{p}$ as follows

$$\frac{\partial p_i}{\partial t} + \frac{\partial (p_j u_j - w)}{\partial x_i} + u_j \left(\frac{\partial p_i}{\partial x_j} - \frac{\partial p_j}{\partial x_i} \right) + b_c \varepsilon_{ijk} \frac{\partial \psi_k}{\partial x_j} = 0, \tag{12a}$$

$$\frac{\partial \psi_i}{\partial t} + u_j \frac{\partial \psi_i}{\partial x_j} - \frac{\gamma}{\rho} b_c \varepsilon_{ijk} \frac{\partial p_k}{\partial x_j} = 0. \tag{12b}$$

The choice of the terms multiplying the curl products is not arbitrary, as the presented form is required for the energy conservation as proven in Appendix A. The total energy for our system, accounting for the cleaning contribution is given by

$$E = \frac{\rho}{2}|\mathbf{u}|^2 + W(\rho) + \frac{\rho}{4} c_s^2 \mathrm{dev}\mathbf{G} : \mathrm{dev}\mathbf{G} + \frac{\gamma}{2}|\mathbf{p}|^2 + \frac{1}{2\alpha\rho}(\rho - \eta)^2 + \frac{\beta}{2}\rho w^2 + \frac{\rho}{2}|\boldsymbol{\psi}|^2. \tag{13}$$

The addition of the cleaning term in the energy is necessary for thermodynamic compatibility and its form allows for it to be appended in the Lagrangian (11) without altering the corresponding Euler-Lagrange equations, thus conserving the variational structure. Accounting for the GLM curl cleaning modifications, an additional scalar balance law for the total energy can be obtained as a consequence of the governing equations and which writes as

$$\partial_t E + \nabla \cdot (E \cdot \mathbf{u} - \mathbf{T} \cdot \mathbf{u} - \gamma w \mathbf{p} + \gamma b_c \, \boldsymbol{\psi} \times \mathbf{p}) = -3 \frac{\det(\mathbf{A})^{5/3}}{\rho \tau c_s^2} \mathcal{E}_{\mathbf{A}} : \mathcal{E}_{\mathbf{A}} \tag{14}$$

where $\mathbf{T} = \Sigma + \mathbf{K} - P \cdot \mathbf{I}$ is the total stress tensor. Compared to classical models of dispersionless hydrodynamics, there are two additional contributions in the energy flux which are due to interstitial working[52] and curl-cleaning energy flux [20] respectively. The former is typical of second gradient continua while the latter appears essentially when evolution equations are coupled through curl terms, which is typically the case in electrodynamics, see for example [49].

In what follows we shall refer to the equations (8), supplemented with the GLM curl-cleaning modifications (12) as the Hyperbolic Navier-Stokes-Korteweg (HNSK) system.

2.3. Hyperbolicity and characteristic velocities

The HNSK system is not straightforward to analyze in its general form, especially when all the space dimensions are taken into account. However, some considerations of practical interest can fairly reduce the

complexity of the task and give further insight into the behavior of the full system. Thus, let us proceed by first considering the one-dimensional case.

2.3.1. One-dimensional analysis

We consider here that all degrees of freedom are functions of t and x that is $\partial_y \equiv \partial_z \equiv 0$. We also assume that $\mathbf{u} = (u_1, 0, 0)^T$ and $\mathbf{p} = (p_1, 0, 0)^T$. In this setting, the HNSK equations can be cast into the quasi-linear form

$$\mathbf{Q}_t + \mathbf{B}(\mathbf{Q})\mathbf{Q}_x = \mathbf{S}(\mathbf{Q}) \tag{15}$$

where $\mathbf{Q} = (\rho, u_1, \eta, w, p_1, A_{11}, A_{22}, A_{33}, \psi_1, \psi_2, \psi_3, A_{12}, A_{13}, A_{21}, A_{23}, A_{31}, A_{32})^T$ is the vector of primitive variables, $\mathbf{S} = \mathbf{S}(\mathbf{Q})$ contains the algebraic source terms and $\mathbf{B}(\mathbf{Q})$ is the system matrix which contains the Jacobian of the flux vector. In an attempt to simplify the algebra, we further suppose that $\mathbf{A} = \mathbf{I}$, so that the system matrix writes

$$\mathbf{B}(\mathbf{Q}) = \begin{pmatrix}
u_1 & \rho & 0 & 0 & 0 & 0 & 0 & 0 & 0 & \dots & 0 \\
\frac{P'(\rho)}{\rho} + \frac{\eta^2}{\alpha\rho^3} & u_1 & \frac{\rho - 2\eta}{\alpha\rho^2} & 0 & \frac{\gamma p_1}{\rho} & \frac{4}{3}cs^2 & -\frac{2}{3}cs^2 & -\frac{2}{3}cs^2 & 0 & \dots & 0 \\
0 & 0 & u_1 & 0 & 0 & 0 & 0 & 0 & 0 & \dots & 0 \\
0 & 0 & 0 & u_1 & -\frac{\gamma}{\beta\rho} & 0 & 0 & 0 & 0 & \dots & 0 \\
0 & p_1 & 0 & -1 & u_1 & 0 & 0 & 0 & 0 & \dots & 0 \\
0 & 1 & 0 & 0 & 0 & u_1 & 0 & 0 & 0 & \dots & 0 \\
0 & 0 & 0 & 0 & 0 & 0 & u_1 & 0 & 0 & \dots & 0 \\
0 & 0 & 0 & 0 & 0 & 0 & 0 & u_1 & 0 & \dots & 0 \\
0 & 0 & 0 & 0 & 0 & 0 & 0 & 0 & u_1 & \dots & 0 \\
\vdots & \vdots & \vdots & \vdots & \vdots & \vdots & \vdots & \vdots & \vdots & \ddots & \vdots \\
0 & 0 & 0 & 0 & 0 & 0 & 0 & 0 & 0 & \dots & u_1
\end{pmatrix} \tag{16}$$

$\mathbf{B}$ admits 17 eigenvalues λ_{1-17} whose expressions are given as follows

$$\begin{cases}
\lambda_{1-13} = u_1, \\
\lambda_{14} = u_1 - \sqrt{Z_1 + Z_2} \\
\lambda_{16} = u_1 - \sqrt{Z_1 - Z_2} \\
\lambda_{15} = u_1 + \sqrt{Z_1 + Z_2} \\
\lambda_{17} = u_1 + \sqrt{Z_1 - Z_2}
\end{cases}, \quad \text{with} \quad
\begin{cases}
Z_1 = \frac{1}{2}(a_0^2 + a_s^2 + a_\gamma^2 + a_\alpha^2 + a_\beta^2), \\
Z_2 = \sqrt{Z_1^2 - a_\beta^2(a_0^2 + a_\alpha^2 + a_s^2)}, \\
a_0 = \sqrt{\rho W''(\rho)}, \quad a_s = \sqrt{\frac{4}{3}c_s^2} \\
a_\alpha = \frac{\eta}{\rho\sqrt{\alpha}}, \quad a_\beta = \sqrt{\frac{\gamma}{\beta\rho}}, \quad a_\gamma = \sqrt{\frac{\gamma}{\rho}p_1^2}
\end{cases} \tag{17}$$

In these expressions, a_0 will be referred to as the adiabatic sound speed as in the Euler subsystem in equations (1), even if the definition itself only holds in the convex regions of $W(\rho)$. a_s is related to the shear sound speed c_s, while a_α, a_β and a_γ are of dispersive origin. More precisely, a_α and a_β can be seen as relaxation wave speeds, while a_γ can be regarded as a characteristic speed of capillary nature. As is typically the case for hyperbolic systems with stiff relaxation terms, the characteristic speeds listed above are not representative of the sound speed in the medium. Indeed, they contain additional contributions of dispersive and viscous nature, that are nevertheless modeled by waves propagating at fast, yet bounded velocities. In order to show that this system is hyperbolic, let us first prove that all the eigenvalues are real for a reasonable choice of the parameters, regardless of the convexity of F. It suffices to prove that $Z_1 \geq 0, Z_2 \geq 0$ and that $Z_1 - Z_2 \geq 0$. Clearly, it is enough to choose, for example, the relaxation parameters α and/or β small enough such that $a_0^2 + a_\alpha^2 + a_\beta^2 > 0$. More precisely, choosing the penalty parameters α and/or β in the augmented Lagrangian approach small enough allows to restore hyperbolicity of the system even in regions where the square of the sound speed $a_0^2 = \rho W''(\rho)$ becomes negative in the case of non-convex equations of state, like the van der Waals equation used in this paper. For $a_0^2 + a_\alpha^2 + a_\beta^2 > 0$ it follows trivially that both $Z_1 \geq 0$ and $Z_1 - Z_2 \geq 0$. Furthermore, basic algebra allows to rewrite Z_2 in the form

$$Z_2 = \sqrt{(Z_1 - a_\beta^2)^2 + a_\beta^2 a_\gamma^2} \geq 0,$$

thus the system of equations (8) accounting for the cleaning (12) is at least weakly hyperbolic under the previous considerations. Besides, it is possible to compute a full basis of right eigenvectors, collected below as the columns of the following matrices, indexed in the same order as their corresponding eigenvalues

$$\mathbf{R}_{1-17} = \begin{pmatrix}
0 & 0 & 0 & 0 & 0 & 0 & 0 & 0 & 0 & r_1 & r_1 & -2r_1 & r_2 & \rho & \rho & \rho & \rho \\
0 & 0 & 0 & 0 & 0 & 0 & 0 & 0 & 0 & 0 & 0 & 0 & 0 & -r_3^+ & -r_3^- & r_3^+ & r_3^- \\
0 & 0 & 0 & 0 & 0 & 0 & 0 & 0 & 0 & 0 & 0 & 0 & 1 & 0 & 0 & 0 & 0 \\
0 & 0 & 0 & 0 & 0 & 0 & 0 & 0 & 0 & 0 & 0 & 0 & 0 & r_4^+ & r_4^- & -r_4^+ & -r_4^- \\
0 & 0 & 0 & 0 & 0 & 0 & 0 & 0 & 0 & 0 & 0 & 0 & 0 & r_5^- & -r_5^+ & r_5^- & -r_5^+ \\
0 & 0 & 0 & 0 & 0 & 0 & 0 & 0 & 0 & 0 & 0 & 1 & 0 & 1 & 1 & 1 & 1 \\
0 & 0 & 0 & 0 & 0 & 0 & 0 & 0 & 0 & 0 & 1 & 0 & 0 & 0 & 0 & 0 & 0 \\
0 & 0 & 0 & 0 & 0 & 0 & 0 & 0 & 0 & 1 & 0 & 0 & 0 & 0 & 0 & 0 & 0 \\
0 & 0 & 0 & 0 & 0 & 0 & 0 & 0 & 1 & 0 & 0 & 0 & 0 & 0 & 0 & 0 & 0 \\
0 & 0 & 0 & 0 & 0 & 0 & 0 & 1 & 0 & 0 & 0 & 0 & 0 & 0 & 0 & 0 & 0 \\
0 & 0 & 0 & 0 & 0 & 0 & 1 & 0 & 0 & 0 & 0 & 0 & 0 & 0 & 0 & 0 & 0 \\
0 & 0 & 0 & 0 & 0 & 1 & 0 & 0 & 0 & 0 & 0 & 0 & 0 & 0 & 0 & 0 & 0 \\
0 & 0 & 0 & 0 & 1 & 0 & 0 & 0 & 0 & 0 & 0 & 0 & 0 & 0 & 0 & 0 & 0 \\
0 & 0 & 0 & 1 & 0 & 0 & 0 & 0 & 0 & 0 & 0 & 0 & 0 & 0 & 0 & 0 & 0 \\
0 & 0 & 1 & 0 & 0 & 0 & 0 & 0 & 0 & 0 & 0 & 0 & 0 & 0 & 0 & 0 & 0 \\
0 & 1 & 0 & 0 & 0 & 0 & 0 & 0 & 0 & 0 & 0 & 0 & 0 & 0 & 0 & 0 & 0 \\
1 & 0 & 0 & 0 & 0 & 0 & 0 & 0 & 0 & 0 & 0 & 0 & 0 & 0 & 0 & 0 & 0
\end{pmatrix}$$

where auxiliary quantities were introduced to lighten the expressions, and which are all given below

$$r_1 = \frac{\rho a_s^2}{2(a^2 + a_\alpha^2)},\ r_2 = \frac{2\eta - \rho}{\alpha\rho(a^2 + a_\alpha^2)},\ r_3^\pm = \sqrt{Z_1 \pm Z_2},\ r_4^\pm = \frac{\sqrt{Z_1 \pm Z_2}(Z_1 - Z_3)}{Z_3 \pm Z_2} p_1,\ r_5^\pm = \frac{(Z_2 \pm Z_4)}{Z_3 - Z_4} p_1$$

$$Z_3 = \frac{1}{2}(a_0^2 + a_s^2 + a_\alpha^2 + a_\gamma^2 - a_\beta^2), \quad Z_4 = \frac{1}{2}(a_0^2 + a_s^2 + a_\alpha^2 - a_\gamma^2 - a_\beta^2)$$

The eigenvectors $\mathbf{R}_{1-13}$ associated to the transport eigenvalue u_1 are trivially linearly independent. However, a similar conclusion is less straightforward for $\mathbf{R}_{14-17}$. In fact, it is more convenient to discuss two separate cases depending on whether Z_2 is equal to zero or not. The condition $Z_2 = 0$ is met if and only if the equalities $a_\gamma = 0$ and $a_\beta^2 = a_0^2 + a_s^2 + a_\alpha^2$ are simultaneously satisfied. In terms of the models' parameters this is equivalent to

$$p_1 = 0, \quad \rho W''(\rho) + \frac{4}{3} c_s^2 + \frac{\eta}{\rho\alpha} = \frac{\gamma}{\beta\rho}. \tag{18}$$

In the case $Z_2 > 0$, the eigenvalues λ_{14-17} are all distinct. It ensues that the eigenvectors $\mathbf{R}_{1-17}$ are all linearly independent and the system is therefore strongly hyperbolic. In the case $Z_2 = 0$, the eigenvalues λ_{14-17} are no longer distinct, as some of them merge as follows:

$$\lambda_{1-13} = u_1, \quad \lambda_{14,15} = u_1 - \sqrt{Z_1}, \quad \lambda_{16,17} = u_1 + \sqrt{Z_1}. \tag{19}$$

Nevertheless, one can still compute a linearly independent basis of eigenvectors for the matrix $\mathbf{B}(\mathbf{Q})$ where p_1 and $\frac{\gamma}{\beta\rho}$ are *a priori* replaced according to their respective values given in (18). This allows to obtain the

following matrix of eigenvectors

$$\mathbf{R'}_{1-17} = \begin{pmatrix}
0 & 0 & 0 & 0 & 0 & 0 & 0 & 0 & 0 & r_1 & r_1 & -2r_1 & r_2 & \rho & 0 & \rho & 0 \\
0 & 0 & 0 & 0 & 0 & 0 & 0 & 0 & 0 & 0 & 0 & 0 & 0 & -a_\beta & 0 & a_\beta & 0 \\
0 & 0 & 0 & 0 & 0 & 0 & 0 & 0 & 0 & 0 & 0 & 0 & 1 & 0 & 0 & 0 & 0 \\
0 & 0 & 0 & 0 & 0 & 0 & 0 & 0 & 0 & 0 & 0 & 0 & 0 & 0 & a_\beta & 0 & -a_\beta \\
0 & 0 & 0 & 0 & 0 & 0 & 0 & 0 & 0 & 0 & 0 & 0 & 0 & 0 & 1 & 0 & 1 \\
0 & 0 & 0 & 0 & 0 & 0 & 0 & 0 & 0 & 0 & 0 & 1 & 0 & 1 & 0 & 1 & 0 \\
0 & 0 & 0 & 0 & 0 & 0 & 0 & 0 & 0 & 0 & 1 & 0 & 0 & 0 & 0 & 0 & 0 \\
0 & 0 & 0 & 0 & 0 & 0 & 0 & 0 & 0 & 1 & 0 & 0 & 0 & 0 & 0 & 0 & 0 \\
0 & 0 & 0 & 0 & 0 & 0 & 0 & 0 & 1 & 0 & 0 & 0 & 0 & 0 & 0 & 0 & 0 \\
0 & 0 & 0 & 0 & 0 & 0 & 0 & 1 & 0 & 0 & 0 & 0 & 0 & 0 & 0 & 0 & 0 \\
0 & 0 & 0 & 0 & 0 & 0 & 1 & 0 & 0 & 0 & 0 & 0 & 0 & 0 & 0 & 0 & 0 \\
0 & 0 & 0 & 0 & 0 & 1 & 0 & 0 & 0 & 0 & 0 & 0 & 0 & 0 & 0 & 0 & 0 \\
0 & 0 & 0 & 0 & 1 & 0 & 0 & 0 & 0 & 0 & 0 & 0 & 0 & 0 & 0 & 0 & 0 \\
0 & 0 & 0 & 1 & 0 & 0 & 0 & 0 & 0 & 0 & 0 & 0 & 0 & 0 & 0 & 0 & 0 \\
0 & 0 & 1 & 0 & 0 & 0 & 0 & 0 & 0 & 0 & 0 & 0 & 0 & 0 & 0 & 0 & 0 \\
0 & 1 & 0 & 0 & 0 & 0 & 0 & 0 & 0 & 0 & 0 & 0 & 0 & 0 & 0 & 0 & 0 \\
1 & 0 & 0 & 0 & 0 & 0 & 0 & 0 & 0 & 0 & 0 & 0 & 0 & 0 & 0 & 0 & 0
\end{pmatrix}$$

which are always linearly independent given that

$$\det(\mathbf{R'}_{1-17}) = -4\rho a_\beta^2 (1 + \frac{a_s}{(a + a_\alpha)}) < 0. \tag{20}$$

Thus, the system of equations (8) with GLM curl cleaning (12) is always hyperbolic in one dimension of space, provided that the parameters α and β are taken such that $a + a_\alpha + a_\beta > 0$.

2.3.2. Multidimensional analysis

A thorough analysis of hyperbolicity in three space dimensions is by no means trivial. Therefore, we shall consider a slightly simplified version for which it is possible to recover meaningful information on the eigenstructure. The geometric properties of our system, in particular its invariance by rotation, allows to reduce the task of checking multidimensional hyperbolicity to the one dimensional case where all variables depend only on the space coordinate x and the time t, but all the components of the vector fields are kept [33]. Under the same notations as in the previous subsection, this allows us to cast the system into the quasilinear form (15) where the vector of primitive variables is now given by $\mathbf{Q} = (\rho, u_1, u_2, u_3, \eta, w, p_1, p_2, p_3, A_{11}, A_{22}, A_{33}, \psi_1, \psi_2, \psi_3, A_{12}, A_{13}, A_{21}, A_{23}, A_{31}, A_{32})^T$. For the purpose of our analysis, we shall linearize the system around a reference state $\mathbf{Q}_0$ such that $\mathbf{A} = \mathbf{I}$ and $\mathbf{p} = (p_1, 0, 0)^T$. The system matrix $\mathbf{B}(\mathbf{Q}_0)$ under these considerations, can be written in a block from as follows

$$\mathbf{B}(\mathbf{Q}_0) = \begin{pmatrix}
\mathbf{B}_1 & \mathbf{C}_1 & \mathbf{C}_2 \\
\mathbf{O}_{4,9} & \mathbf{B}_2 & \mathbf{O}_{4,8} \\
\mathbf{O}_{8,9} & \mathbf{O}_{8,4} & \mathbf{I}_8
\end{pmatrix} \tag{21}$$

where the matrices $\mathbf{I}_n$ and $\mathbf{O}_{n,m}$ denote the $n \times n$ identity matrix and the $n \times m$ zero matrix respectively and the blocks $\mathbf{B}_1$, $\mathbf{B}_2$, $\mathbf{C}_1$ and $\mathbf{C}_2$ are defined below

$$\mathbf{B}_1 = \begin{pmatrix} u_1 & \rho & 0 & 0 & 0 & 0 & 0 & 0 & 0 \\ \frac{a_\alpha^2+a_0^2}{\rho} & u_1 & 0 & 0 & \frac{4c_s^2}{3} & 0 & 0 & 0 & \frac{a_\gamma^2}{p_1} \\ 0 & 0 & u_1 & 0 & 0 & c_s^2 & 0 & 0 & 0 \\ 0 & 0 & 0 & u_1 & 0 & 0 & c_s^2 & 0 & 0 \\ 0 & 1 & 0 & 0 & u_1 & 0 & 0 & 0 & 0 \\ 0 & 0 & 1 & 0 & 0 & u_1 & 0 & 0 & 0 \\ 0 & 0 & 0 & 1 & 0 & 0 & u_1 & 0 & 0 \\ 0 & 0 & 0 & 0 & 0 & 0 & 0 & u_1 & -a_\beta^2 \\ 0 & p_1 & 0 & 0 & 0 & 0 & 0 & -1 & u_1 \end{pmatrix}, \quad \mathbf{B}_2 = \begin{pmatrix} u_1 & 0 & -b_c & 0 \\ 0 & u_1 & 0 & b_c \\ -\frac{b_c\gamma}{\rho} & 0 & u_1 & 0 \\ 0 & \frac{b_c\gamma}{\rho} & 0 & u_1 \end{pmatrix}.$$

$$\mathbf{C}_1 = \begin{pmatrix} 0 & 0 & 0 & 0 \\ 0 & 0 & 0 & 0 \\ 0 & 0 & 0 & 0 \\ 0 & 0 & 0 & 0 \\ \frac{a_\gamma^2}{p_1} & 0 & 0 & 0 \\ 0 & \frac{a_\gamma^2}{p_1} & 0 & 0 \\ 0 & 0 & 0 & 0 \\ 0 & 0 & 0 & 0 \\ 0 & 0 & 0 & 0 \end{pmatrix}, \quad \mathbf{C}_2 = \begin{pmatrix} 0 & 0 & 0 & 0 & 0 & 0 & 0 & 0 \\ 0 & 0 & 0 & 0 & 0 & 0 & 0 & 0 \\ 0 & 0 & 0 & 0 & 0 & 0 & 0 & 0 \\ \frac{\rho-2\eta}{\alpha\rho^2} & -\frac{2c_s^2}{3} & 0 & 0 & -\frac{2c_s^2}{3} & 0 & 0 & 0 \\ 0 & 0 & c_s^2 & 0 & 0 & 0 & 0 & 0 \\ 0 & 0 & 0 & c_s^2 & 0 & 0 & 0 & 0 \\ 0 & 0 & 0 & 0 & 0 & 0 & 0 & 0 \\ 0 & 0 & 0 & 0 & 0 & 0 & 0 & 0 \\ 0 & 0 & 0 & 0 & 0 & 0 & 0 & 0 \end{pmatrix}$$

By virtue of the block decomposition (21), the eigenvalues of $\mathbf{B}(\mathbf{Q}_0)$ can be seen as the union of eigenvalues for each of the blocks $\mathbf{B}_1$, $\mathbf{B}_2$ and $\mathbf{I}_8$ and which are regrouped here, under the previous notations

$$\lambda_{1-9} = u_1, \quad \begin{cases} \lambda_{10-11} = u_1 + c_s, \\ \lambda_{12-13} = u_1 - c_s, \end{cases}, \begin{cases} \lambda_{14-15} = u_1 - a_c, \\ \lambda_{16-17} = u_1 + a_c, \end{cases} \quad \begin{cases} \lambda_{18} = u_1 - \sqrt{Z_1 + Z_2} \\ \lambda_{19} = u_1 - \sqrt{Z_1 - Z_2} \\ \lambda_{20} = u_1 + \sqrt{Z_1 + Z_2} \\ \lambda_{21} = u_1 + \sqrt{Z_1 - Z_2} \end{cases} \tag{22}$$

The characteristics λ_{1-9} correspond to passive transport, λ_{10-13} correspond to the shear waves, λ_{14-17} represent the GLM curl-cleaning waves where the cleaning speed is given by $a_c = \sqrt{\frac{\gamma}{\rho}} b_c$ and λ_{17-21} are the longitudinal characteristic speeds and which in this case contain the main couplings between the viscous and dispersive effects as well as the pressure waves. The corresponding eigenvectors are given below separately

for each set of eigenvalues

$$\mathbf{R}_{1-9} = \begin{pmatrix} 0 & 0 & 0 & r_1 & 0 & 0 & r_1 & r_2 & -r_1 \\ 0 & 0 & 0 & 0 & 0 & 0 & 0 & 0 & 0 \\ 0 & 0 & 0 & 0 & 0 & 0 & 0 & 0 & 0 \\ 0 & 0 & 0 & 0 & 0 & 0 & 0 & 0 & 0 \\ 0 & 0 & 0 & 0 & 0 & 0 & 0 & 0 & 1 \\ 0 & 0 & 0 & 0 & 0 & -1 & 0 & 0 & 0 \\ 0 & 0 & 0 & 0 & -1 & 0 & 0 & 0 & 0 \\ 0 & 0 & 0 & 0 & 0 & 0 & 0 & 0 & 0 \\ 0 & 0 & 0 & 0 & 0 & 0 & 0 & 0 & 0 \\ 0 & 0 & 0 & 0 & 0 & 0 & 0 & 0 & 0 \\ 0 & 0 & 0 & 0 & 0 & 0 & 0 & 0 & 0 \\ 0 & 0 & 0 & 0 & 0 & 0 & 0 & 0 & 0 \\ 0 & 0 & 0 & 0 & 0 & 0 & 0 & 1 & 0 \\ 0 & 0 & 0 & 0 & 0 & 0 & 1 & 0 & 0 \\ 0 & 0 & 0 & 0 & 0 & 1 & 0 & 0 & 0 \\ 0 & 0 & 0 & 0 & 1 & 0 & 0 & 0 & 0 \\ 0 & 0 & 0 & 1 & 0 & 0 & 0 & 0 & 0 \\ 0 & 0 & 1 & 0 & 0 & 0 & 0 & 0 & 0 \\ 0 & 1 & 0 & 0 & 0 & 0 & 0 & 0 & 0 \\ 1 & 0 & 0 & 0 & 0 & 0 & 0 & 0 & 0 \end{pmatrix}, \mathbf{R}_{10-13} = \begin{pmatrix} 0 & 0 & 0 & 0 \\ 0 & 0 & 0 & 0 \\ 0 & c_s & 0 & -c_s \\ c_s & 0 & -c_s & 0 \\ 0 & 0 & 0 & 0 \\ 0 & 1 & 0 & 1 \\ 1 & 0 & 1 & 0 \\ 0 & 0 & 0 & 0 \\ 0 & 0 & 0 & 0 \\ 0 & 0 & 0 & 0 \\ 0 & 0 & 0 & 0 \\ 0 & 0 & 0 & 0 \\ 0 & 0 & 0 & 0 \\ 0 & 0 & 0 & 0 \\ 0 & 0 & 0 & 0 \\ 0 & 0 & 0 & 0 \\ 0 & 0 & 0 & 0 \\ 0 & 0 & 0 & 0 \\ 0 & 0 & 0 & 0 \end{pmatrix},$$

$$\mathbf{R}_{14-17} = \begin{pmatrix} 0 & 0 & 0 & 0 \\ 0 & 0 & 0 & 0 \\ 0 & -r_6 a_c & 0 & -r_6 a_c \\ r_6 a_c & 0 & r_6 a_c & 0 \\ 0 & 0 & 0 & 0 \\ 0 & r_6 & 0 & -r_6 \\ -r_6 & 0 & r_6 & 0 \\ 0 & 0 & 0 & 0 \\ 0 & 0 & 0 & 0 \\ 0 & \sqrt{\frac{\rho}{\gamma}} & 0 & -\sqrt{\frac{\rho}{\gamma}} \\ -\sqrt{\frac{\rho}{\gamma}} & 0 & \sqrt{\frac{\rho}{\gamma}} & 0 \\ 0 & 1 & 0 & 1 \\ 1 & 0 & 1 & 0 \\ 0 & 0 & 0 & 0 \\ 0 & 0 & 0 & 0 \\ 0 & 0 & 0 & 0 \\ 0 & 0 & 0 & 0 \\ 0 & 0 & 0 & 0 \\ 0 & 0 & 0 & 0 \\ 0 & 0 & 0 & 0 \\ 0 & 0 & 0 & 0 \end{pmatrix}, \quad \mathbf{R}_{18-21} = \begin{pmatrix} r_7^+ & r_7^+ & r_7^- & r_7^- \\ -r_8^+ & r_8^+ & r_8^- & -r_8^- \\ 0 & 0 & 0 & 0 \\ 0 & 0 & 0 & 0 \\ r_9^+ & r_9^+ & r_9^- & r_9^- \\ 0 & 0 & 0 & 0 \\ 0 & 0 & 0 & 0 \\ \frac{a\beta^2}{r_3^+} & -\frac{a\beta^2}{r_3^+} & \frac{a\beta^2}{r_3^-} & -\frac{a\beta^2}{r_3^-} \\ 1 & 1 & 1 & 1 \\ 0 & 0 & 0 & 0 \\ 0 & 0 & 0 & 0 \\ 0 & 0 & 0 & 0 \\ 0 & 0 & 0 & 0 \\ 0 & 0 & 0 & 0 \\ 0 & 0 & 0 & 0 \\ 0 & 0 & 0 & 0 \\ 0 & 0 & 0 & 0 \\ 0 & 0 & 0 & 0 \\ 0 & 0 & 0 & 0 \\ 0 & 0 & 0 & 0 \\ 0 & 0 & 0 & 0 \end{pmatrix}$$

where

$$r_6 = \frac{1}{a_c^2 - cs^2}\sqrt{\frac{\gamma}{\rho}}p_1, \quad r_7^{\pm} = \frac{\rho}{p_1}\frac{Z_2 \pm Z_4}{Z_1 + Z_4}, \quad r_8^{\pm} = \frac{1}{p_1}\frac{Z_2 \pm Z_3}{\sqrt{Z_1 \pm Z_2}}, \quad r_9^{\pm} = \frac{1}{p_1}\frac{Z_4 \pm Z_2}{Z_1 + Z_4}$$

The eigenvectors $\mathbf{R}_{1-17}$ are clearly linearly independent. Concerning $\mathbf{R}_{18-21}$, both the eigenvectors and their corresponding eigenvalues show a very similar structure to the one-dimensional case. Hyperbolicity follows by virtue of the same analysis.

2.4. Dispersion relation

For systems with inherent dissipation and dispersion, it is fundamental to compute the dispersion relation as it assesses how waves propagate and decay as a function of the wavelength. For that, we linearize equation (15) around an equilibrium state $\mathbf{Q}_0$ defined by $\rho = \eta = \rho_0$, $\mathbf{p} = 0$, $\mathbf{u} = 0$, $\mathbf{A} = \mathbf{I}$, $w = 0$ and $\boldsymbol{\psi} = 0$, and we look for harmonic plane wave solutions of the form $\mathbf{Q} = \mathbf{Q}_0 + \mathbf{Q}_\epsilon e^{i(kx-\omega t)}$, where i is the complex unity, k is the wavenumber and ω is the complex frequency. In order to obtain the phase velocity and the decay rate of the system, we define the auxiliary quantity $z = \omega/k$, which for our system can be obtained as a root of the equation

$$P(z) = \det\left(\mathbf{B}(\mathbf{Q}_0) + \frac{i}{k}\frac{\partial \mathbf{S}}{\partial \mathbf{Q}} - z\,\mathbf{I}\right) = 0. \tag{23}$$

The phase velocity c_p and the decay rate d are then obtained from z as

$$c_p(k) = \mathrm{Re}(z), \quad d(k) = -k\,\mathrm{Im}(z). \tag{24}$$

For the hyperbolic NSK model, equation (23) admits 21 complex roots z_{1-21} and obtaining an explicit expression for all of them is a rather arduous exercise of algebra. Nevertheless, we present hereafter an exact expression for z_{1-17} and which write

$$z_{1-6} = 0,\ z_{7-8} = -\frac{6i}{k\tau}, \quad \begin{cases} z_{9-10} = -a_c, \\ z_{11-12} = ac \end{cases}, \quad \begin{cases} z_{13-14} = -\frac{3i}{k\tau} - \sqrt{c_s^2 - \frac{9}{k^2\tau^2}}, \\ z_{15-16} = -\frac{3i}{k\tau} + \sqrt{c_s^2 - \frac{9}{k^2\tau^2}} \end{cases}. \tag{25}$$

The five remaining values z_{17-21} can be defined as the roots of a fifth degree polynomial $P_5(z)$ that remains after division of (23) by the factors $z - z_k$, $k \in \{1, 2, \ldots, 16\}$, i.e.

$$P_5(z) = \frac{P(z)}{\prod_{k=1}^{16}(z - z_k)} = 0. \tag{26}$$

Nevertheless, although no explicit expression has been obtained, it is possible to solve the problem $P_5(z) = 0$ *numerically* in order to obtain relevant information on their behavior. A plot of the phase velocities $c_{p,17-21}$ and the decay rates d_{17-21} is given along their corresponding values for the original Navier-Stokes-Korteweg equations in Figure 2. The dispersion relation of the original NSK system is recalled here

$$z_{1,2} = -\frac{2i\mu k}{3\rho} \pm \sqrt{\rho W''(\rho) + \left(\gamma\rho - \frac{4\mu^2}{9\rho^2}\right)k^2}, \quad z_{3,4} = -\frac{ik\mu}{\rho}, \tag{27}$$

and from where we can recover the phase velocity $\tilde{c}_p = |\mathrm{Re}(z_{1,2})|$ and the decay rate $\tilde{d} = -k\,\mathrm{Im}(z_{1,2})$, which will serve later as a reference. Note that large values of the viscosity μ may lead to the suppression of dispersive effects in particular for $\mu \geq \frac{2}{3}\sqrt{\gamma\rho^3}$. The phase velocity plot in Figure 2 shows that out of the roots z_{17-21}, $z_{18,20}$ are asymptotically equivalent to the Navier-Stokes-Korteweg system in the vicinity of the long-wave limit $k \to 0$. However, there exists necessarily a cut-off wavenumber, say k_c, starting from which, the curves begin to diverge from one another. This comes as no surprise since in the short-wave limit, that is $k \to \infty$, we have $\tilde{c}_p \to \infty$ whereas for a hyperbolic system of equations, phase velocities remain bounded and converge to their corresponding characteristics in the same limit, thus giving a non-uniform convergence. A similar behavior is observed for the decay rates, as $\tilde{d}$ is very well-captured by d_{18} and d_{20}

for the long waves up to k_c. This threshold is expected to to increase in the stiff relaxation limits $\alpha \to 0$, $\beta \to 0$ and $c_s \to \infty$, thus expanding the region of correspondence of our model with the NSK equations to higher frequencies. However, in the presence of multiple relaxations of different physical nature, it seems necessary to impose a scaling of the governing relaxation parameters, as the analysis might otherwise lead to an erroneous interpretation.

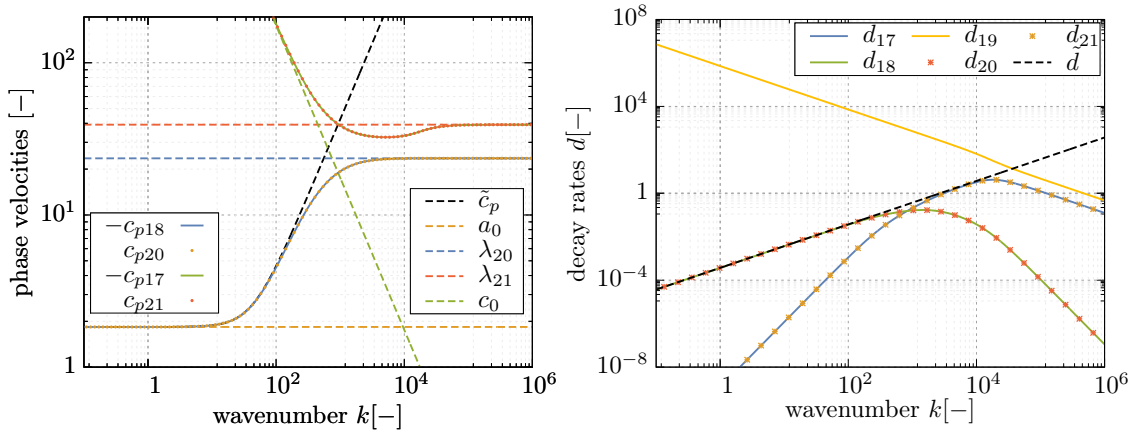

Figure 2: Plot of the phase velocities cp_{17-21} (left) and the decay rates d_{17-21} along their counterparts for the Navier-Stokes-Korteweg system. For both figures, a continuous brown line corresponds to the original NSK. The values of the parameters are $\alpha = 10^{-3}$, $\beta = 10^{-5}$, $\gamma = 10^{-3}$, $\mu = 10^{-3}$, $cs = 20$, $\rho = 1.8$

As such, we base our scaling on the characteristic speeds, since they provide some insight into the different velocities involved by the relaxation mechanisms and which we identified in equation (17) as a_α, a_β and a_s. The following scaling

$$\beta(\alpha) = \gamma\alpha, \quad c_s(\alpha) = \sqrt{\frac{1}{\alpha}} \tag{28}$$

allows to reduce the relaxation to a one-parameter process and keeps the corresponding characteristics at the same order of magnitude in the stiff relaxation limit $\alpha \to 0$. In Figure 3 we compare the phase velocity d_{20} and the decay rate d_{20} with the reference NSK values $\tilde{c}_p$ and $\tilde{d}$. The figure shows that for smaller values of α, the region over which both the phase velocity and the decay rate correspond to those of the NSK equations extends to higher values of k.

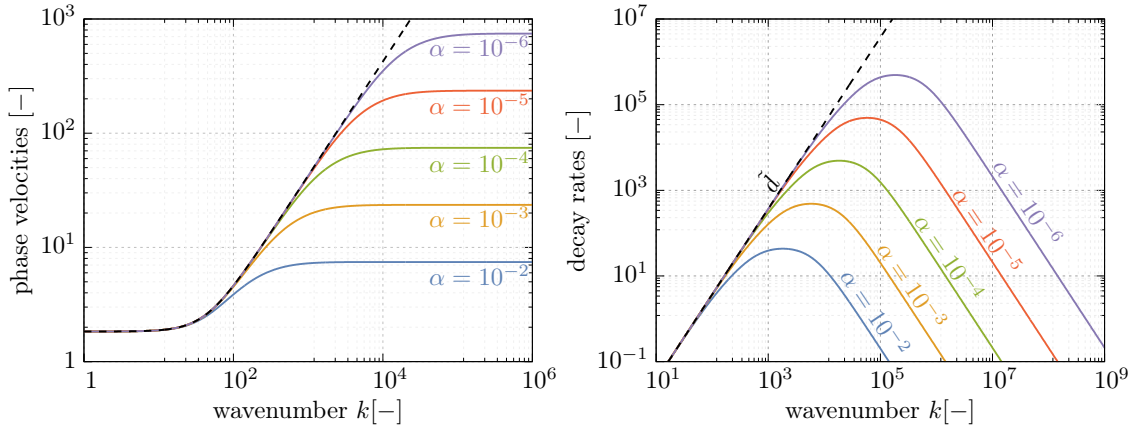

Figure 3: Plot of the phase velocities cp_{20} (left) and the decay rate d_{20} for several values of α along their counterparts for the Navier-Stokes-Korteweg system. For both figures, the dashed black line corresponds to the original NSK while the colored continuous lines correspond to the hyperbolic approximation for different α. The remaining parameters are as follows $\gamma = 10^{-3}$, $\mu = 10^{-3}$ and $\rho = 1.8$

3. Numerical method

The model we present in this paper is a first-order hyperbolic system of equations where non-conservative terms and algebraic sources are present. Thus, in order to present the general framework for the numerical solution, we consider the general form of the PDE to be solved

$$\frac{\partial \mathbf{U}}{\partial t} + \nabla \cdot \mathbf{F}(\mathbf{U}) + \mathbf{B}(\mathbf{U}) \cdot \nabla \mathbf{U} = \mathbf{S}(\mathbf{U}). \tag{29}$$

Here $\mathbf{U} \in \mathbb{R}^m$ is the vector of conserved variables with $m = 12 + 3d$. The tensor $\mathbf{F} \in \mathbb{R}^{m \times d}$ contains the PDE fluxes such that the k^{th} column of $\mathbf{F}$ corresponds to the flux vector in the direction x_k. The non-conservative terms are written in the quasi-linear form $\mathbf{B}(\mathbf{U}) \cdot \nabla \mathbf{U}$ with $\mathbf{B} \in \mathbb{R}^{m \times d}$ and $\mathbf{S} \in \mathbb{R}^m$ is the vector of source terms. The numerical method used here, in its most general form, falls into the category of $\mathbb{P}_N\mathbb{P}_M$ schemes [42, 41, 50, 44, 12], which in general employ a combination of the discontinuous Galerkin framework with finite volumes. The data is represented by polynomials of degree N while the fluxes are obtained from a reconstruction by polynomials of degree $M \geq N$. While in principle, one could use $M > N$, we will use in the rest of the paper $N = M$, which makes the method a one-step fully discrete ADER discontinuous Galerkin scheme , for which a detailed summary is given in the following sections.

3.1. One-step ADER discontinuous Galerkin methods

The approach we recall here finds its foundations in [45, 42] and differs from the classical ADER approach forwarded by Toro and Titarev [74, 75, 76, 24] in the sense that the original approach of Toro and Titarev makes use of the *strong* form of the governing PDE system and the Cauchy-Kowalevskaya procedure in order to replace time derivatives by space derivatives, while the method used in this paper employs a *weak* integral formulation of the PDE in space-time. The approach allows for the treatment of stiff sources and is easily applicable to general nonlinear hyperbolic PDE systems. In all what follows, we present the approach in two dimensions of space, in a format that is easily extendable also to three space dimensions. The notation (x, y) will be used instead of (x_1, x_2) to ease notation. In general, we consider a rectangular domain $[-L_x/2, L_x/2] \times [-L_y/2, L_y/2]$ discretized over a uniform Cartesian grid comprised of $N_x \times N_y$ cells, each occupying a domain $\Omega_i = [x_i - \frac{\Delta x}{2}, x_i + \frac{\Delta x}{2}] \times [y_i - \frac{\Delta x}{2}, y_i + \frac{\Delta y}{2}]$, where (x_i, y_i) are the coordinates of the i^{th} cell's barycenter. The mesh size is such that $\Delta x = L_x/N_x$ and $\Delta y = L_y/N_y$.

In the framework of the ADER discontinuous Galerkin finite element approach, we assume that the numerical solution to the PDE (29) belongs to the space of piece-wise polynomials of degree N, which are

spanned by the basis functions $\varphi_k(x,y)$, $k \in [1,(N+1)^2]$. For simplicity, the basis functions are defined over a fixed interval $[0,1]\times[0,1]$ and the position inside each cell is mapped to the unit square by considering local coordinates (ξ,η) defined by $x = x_i - \frac{\Delta x}{2} + \xi\Delta x$ and $y = y_i - \frac{\Delta y}{2} + \eta\Delta y$, where $0 \le \xi,\eta \le 1$. For the sake of simplicity, a slight abuse of notation will be used so that a given function $f\colon (x,y) \in \Omega_i \to \mathbb{R}$ will still be referred to as $f\colon (\xi,\eta) \in [0,1]^2 \to \mathbb{R}$ regardless of which coordinates are used, and which shall be unambiguously mentioned or given away by the integral boundaries. We proceed by assuming that the numerical solution to the PDE (29) at a time t^n, denoted by $\mathbf{u}_h(x,y,t^n)$, can be expanded in terms of the basis functions in every cell Ω_i as follows

$$\mathbf{u}_h(x,y,t^n) = \varphi_k(x,y)\,\hat{\mathbf{u}}^n_{k,i} \tag{30}$$

Note that the space dependence inside a cell is completely shifted on the basis functions φ_k. As for the choice of the latter, we take an orthogonal nodal basis $\{\varphi_k\}_{k\in\{0,\dots,2N+1\}}$, generated by the tensor product $\{\varphi_{k_1}\varphi_{k_2}\}_{k_1,k_2\in\{0,\dots,N\}}$ where $\{\varphi_{k_i}\}_{k_i,\in\{0,\dots,N\}}$ are Lagrange interpolation polynomials going through $N+1$ Gauss-Legendre quadrature nodes. In the framework of Discontinuous Galerkin methods, equation (29) is multiplied by a test function φ_k and integrated over a space-time control volume $\Omega_i \times [t^n, t^{n+1}]$ to obtain

$$\int_{t^n}^{t^{n+1}}\int_{\Omega_i} \varphi_k \left(\frac{\partial \mathbf{U}}{\partial t} + \nabla\cdot\mathbf{F}(\mathbf{U}) + \mathbf{B}(\mathbf{U})\cdot\nabla\mathbf{U}\right) d\Omega\, dt = \int_{t^n}^{t^{n+1}}\int_{\Omega_i} \varphi_k\,(\mathbf{S}(\mathbf{U}))\, d\Omega\, dt. \tag{31}$$

Inside the control volume, we substitute $\mathbf{U}$ by the numerical solution, expanded as in (30). Since $\hat{\mathbf{u}}^n_{k,i}$ are constant within Ω_i, integration by parts of the left-hand side allows to obtain

$$\begin{aligned}
&\left(\int_{\Omega_i}\phi_k\phi_l\, d\Omega\right)\left(\hat{\mathbf{u}}^{n+1}_{l,i} - \hat{\mathbf{u}}^n_{l,i}\right) + \int_{t^n}^{t^{n+1}}\int_{\partial\Omega_i}\phi_k\left(\mathcal{F}\left(\mathbf{q}_h^-,\mathbf{q}_h^+\right) + \mathcal{D}\left(\mathbf{q}_h^-,\mathbf{q}_h^+\right)\right)\cdot\mathbf{n}\, dS\, dt \\
&- \int_{t^n}^{t^{n+1}}\int_{\Omega_i}\nabla\phi_k\cdot\mathbf{F}(\mathbf{q}_h)\, d\Omega\, dt + \int_{t^n}^{t^{n+1}}\int_{\Omega_i^\circ}\phi_k\mathbf{B}(\mathbf{q}_h)\cdot\nabla\mathbf{q}_h\, d\Omega\, dt = \int_{\Omega_i}\phi_k\mathbf{S}(\mathbf{q}_h)\, d\Omega\, dt,
\end{aligned} \tag{32}$$

where $\mathbf{q_h}$ is the space-time predictor, $\mathbf{q_h}^+$ and $\mathbf{q_h}^-$ refer to its boundary extrapolated values from within Ω_i and Ω_j, j being a generic index of a neighboring cell. Details on the computation of $\mathbf{q}_h$ will be laid out in the next subsection. $\mathbf{n}$ is the normal vector to the cell boundary $\partial\Omega_i$, pointing outwards. The intercell flux is computed at the aid of the Rusanov approximate Riemann solver [77] as follows

$$\mathcal{F}\left(\mathbf{q}_h^-,\mathbf{q}_h^+\right)\cdot\mathbf{n} = \frac{1}{2}\left(\mathbf{F}(\mathbf{q}_h^+) + \mathbf{F}(\mathbf{q}_h^-)\right)\cdot\mathbf{n} - \frac{1}{2}s_{\max}\,\mathbf{I}\left(\mathbf{q}_h^+ - \mathbf{q}_h^-\right), \tag{33}$$

where $s_{max} = \max\left(\left|\lambda_k(\mathbf{q}_h^+)\right|, \left|\lambda_k(\mathbf{q}_h^-)\right|\right)$ is the maximum wave speed at the interface. For the non-conservative product, a path-conservative method [28, 67] is employed here. In this setting, a linear path is chosen

$$\Psi(s,\mathbf{q}_h^+,\mathbf{q}_h^-) = \mathbf{q}_h^- + s(\mathbf{q}_h^+ - \mathbf{q}_h^+), \quad s\in[0,1] \tag{34}$$

so that the non-conservative terms reduce to the following expression

$$\mathcal{D}(\mathbf{q}_h^-,\mathbf{q}_h^+)\cdot\mathbf{n} = \frac{1}{2}\tilde{\mathbf{B}}\cdot(\mathbf{q}_h^+ - \mathbf{q}_h^-), \quad \text{with} \quad \tilde{\mathbf{B}} = \int_0^1 \mathbf{B}(\Psi(s,\mathbf{q}_h^+,\mathbf{q}_h^-))\cdot\mathbf{n}\, dS \tag{35}$$

where the $\tilde{\mathbf{B}}$ is numerically integrated by using Gauss quadrature.

3.2. Local space-time predictor

In order to compute the coefficients $\hat{\mathbf{u}}_{l,i}^{n}$ from equation (32), it is required that the local space-time predictor be computed. The latter is obtained as a solution of a weak local formulation of (29). We consider here space-time basis functions θ_k, that are obtained as the tensor product $\theta_k(\xi,\eta,\tau) = \varphi_{k_0}(\tau)\varphi_{k_1}(\xi)\varphi_{k_2}(\eta)$, of the same previously introduced Lagrange interpolation polynomials and τ is defined in the interval $[0,1]$ similarly to ξ and η, as a local time coordinate so that for every $t \in [t^n, t^{n+1}]$ we have $t = t^n + \tau\Delta t$. The predictor $\mathbf{q}_h$ is then sought in the form

$$\mathbf{q}_h(x,y,t) = \theta_k(x,y,t)\hat{\mathbf{q}}_{k,i}, \tag{36}$$

as a weak solution to (29). Hence, the expansion (36) is inserted into the latter which is then multiplied by a space-time basis function θ_k and integrated over $\Omega_i \times [t^n, t^{n+1}]$ yields

$$\int_{t^n}^{t^{n+1}}\int_{\Omega_i} \theta_k \left(\mathbf{U}_t + \nabla\cdot\mathbf{F}(\mathbf{U}) + \mathbf{B}(\mathbf{U})\cdot\nabla\mathbf{U}\right) d\Omega\, dt = \int_{t^n}^{t^{n+1}}\int_{\Omega_i} \theta_k \left(\mathbf{S}(\mathbf{U})\right) d\Omega\, dt. \tag{37}$$

Integrating by parts only the term containing the time derivative, and taking into account that at time t^n we start from the state $\mathbf{u}_h^n$, this allows to write

$$\begin{aligned}
&\int_{\Omega_i} \theta_k(x,y,t^{n+1})\mathbf{q}_h(x,y,t^{n+1})\, d\Omega - \int_{\Omega_i} \theta_k(x,y,t^n)\mathbf{u}_h(x,y,t^n)\, d\Omega - \int_{t^n}^{t^{n+1}}\int_{\Omega_i} \frac{\partial\theta_k}{\partial t}\,\mathbf{q}_h\, d\Omega\, dt \\
&+ \int_{t^n}^{t^{n+1}}\int_{\Omega_i} \theta_k\,\nabla\cdot\mathbf{F}(\mathbf{q}_h)\, d\Omega\, dt + \int_{t^n}^{t^{n+1}}\int_{\Omega_i^\circ} \theta_k\mathbf{B}(\mathbf{q}_h)\cdot\nabla\mathbf{q}_h\, d\Omega\, dt = \int_{\Omega_i} \theta_k\mathbf{S}(\mathbf{q}_h)\, d\Omega\, dt.
\end{aligned} \tag{38}$$

By expanding the predictor as in (36) one obtains an algebraic equation for $\hat{\mathbf{q}}$, which is solved by a fixed point iteration, the convergence of which was proven for the homogeneous nonlinear case in [18]. Once the predictor is known, equations (32) allows to compute the polynomial coefficients $\hat{\mathbf{u}}^{n+1}$ in every cell, by using Gaussian quadrature for the remaining integrals.

3.3. A posteriori subcell finite volume limiter

The numerical method presented before is high order accurate but *linear* in the sense of Godunov. Therefore, according to the well-known Godunov theorem, it will in general produce spurious oscillations at shock waves and other discontinuities. In [51, 79] a new *a posteriori* subcell limiter was introduced for high order fully-discrete one-step ADER-DG schemes, based on the MOOD paradigm introduced in [31, 39, 40] for finite volume schemes.

At the beginning of each time step, the *unlimited* scheme described in the previous section is run on all cells in order to produce a so-called *candidate solution*, in the following called $\mathbf{u}_h^*(\mathbf{x}, t^{n+1})$. Then, *a posteriori*, the candidate solution is checked against several numerical and physical detection criteria, like the positivity of the density and of η and the absence of floating point errors (`NaN`). We furthermore require that a discrete maximum principle (DMP) is fulfilled, see [51]. If any of these numerical or physical detection criteria is violated inside a DG element, the element is marked as troubled cell and is scheduled for the *a posteriori* subcell finite volume (FV) limiting described below.

The cells Ω_i scheduled for *a posteriori* limiting are now split into $(2N+1)^2$ FV subcells, which are denoted by $\Omega_{i,s}$ with $\Omega_i = \bigcup_s \Omega_{i,s}$. This subdivision of a high order DG element into small subcells does *not* reduce the time step of the DG scheme since the CFL number of explicit DG schemes scales with $1/(2N+1)$, while the maximum Courant number of finite volume methods is unity. At time t^n the discrete

solution is represented in the finite volume subcells $\Omega_{i,s}$ via *piecewise constant* cell averages, denoted by $\bar{\mathbf{u}}_{i,s}^n$ and which are obtained from the high order DG polynomials $\mathbf{u}_h(\mathbf{x}, t^n)$ by simple averaging as

$$\bar{\mathbf{u}}_{i,s}^n = \frac{1}{|\Omega_{i,s}|} \int_{\Omega_{i,s}} \mathbf{u}_h(\mathbf{x}, t^n) d\mathbf{x}. \tag{39}$$

These subcell averages are now either evolved in time at the aid of a second order MUSCL-Hancock-type TVD finite volume scheme with minmod limiter, or at the aid of a third order ADER-WENO finite volume scheme, see [51], which are also both predictor-corrector method and thus looks almost identical to the ADER-DG scheme, apart from the necessary nonlinear reconstruction step. Another major difference is that now the test function is unity, hence the volume integral over the flux term disappears, and the spatial control volumes Ω_i are replaced by the sub-volumes $\Omega_{i,s}$:

$$\begin{aligned} |\Omega_{i,s}| \left(\bar{\mathbf{u}}_{i,s}^{n+1} - \bar{\mathbf{u}}_{i,s}^{n} \right) + \int_{t^n}^{t^{n+1}} \int_{\partial\Omega_{i,s}} \left(\mathcal{G}\left(\mathbf{q}_h^-, \mathbf{q}_h^+\right) + \mathcal{D}\left(\mathbf{q}_h^-, \mathbf{q}_h^+\right) \right) \cdot \mathbf{n} \; dS \; dt \\ + \int_{t^n}^{t^{n+1}} \int_{\Omega_{i,s}^\circ} \left(\mathbf{B}(\mathbf{q}_h) \cdot \nabla \mathbf{q}_h \right) \; d\mathbf{x} \, dt = \int_{t^n}^{t^{n+1}} \int_{\Omega_{i,s}} \mathbf{S}(\mathbf{q}_h, \nabla \mathbf{q}_h) \, d\mathbf{x} \, dt \, . \end{aligned} \tag{40}$$

Once the cell averages $\bar{\mathbf{u}}_{i,s}^{n+1}$ of all subcells in Ω_i have been computed according to (3.3), the limited DG polynomial $\mathbf{u}_h'(\mathbf{x}, t^{n+1})$ at the new time is obtained via a constrained least squares reconstruction, requiring

$$\frac{1}{|\Omega_{i,s}|} \int_{\Omega_{i,s}} \mathbf{u}_h'(\mathbf{x}, t^{n+1}) \, d\mathbf{x} = \bar{\mathbf{u}}_{i,s}^{n+1} \qquad \forall \Omega_{i,s} \in \Omega_i, \tag{41}$$

and

$$\int_{\Omega_i} \mathbf{u}_h'(\mathbf{x}, t^{n+1}) \, d\mathbf{x} = \sum_{\Omega_{i,s} \in \Omega_i} |\Omega_{i,s}| \bar{\mathbf{u}}_{i,s}^{n+1}. \tag{42}$$

The meaning of constraint (42) is conservation of the solution within the element Ω_i. In addition to the expansion coefficients $\hat{\mathbf{u}}_{i,l}^{n+1}$ of the limited DG polynomial, in all limited DG elements we also keep in memory the finite volume subcell averages $\bar{\mathbf{u}}_{i,s}^{n+1}$, since they serve as initial condition for the subcell finite volume limiter in the case when a cell is troubled also in the next time step, see [51]. For more details on the *a posteriori* subcell FV limiter, the reader is referred to [51, 79, 47].

4. Numerical results

In all what follows, whenever the HNSK model is solved numerically, and unless stated otherwise in a specific test description, the following variables will be by default initialized as follows at $t = 0$

$$\mathbf{A} = \mathbf{I}, \quad \eta(\mathbf{x}, 0) = \rho(\mathbf{x}, 0), \quad \mathbf{p}(\mathbf{x}, 0) = \nabla\rho(\mathbf{x}, 0), \quad w(\mathbf{x}, 0) = -\rho \mathrm{div}(\mathbf{u}), \quad \boldsymbol{\psi} = 0. \tag{43}$$

4.1. Convergence analysis in α for a static solution

Equilibrium solutions where both phases coexist can be obtained in one or several dimensions of space. In the setting of the original NSK equations, a stationary solution corresponds to the balance of the pressure gradient with the surface tension forces which results in the following ODE, resulting from the system (1) at equilibrium

$$\nabla P(\rho) = \gamma \rho \nabla \cdot \left(\nabla^2 \rho \right). \tag{44}$$

Similarly, a stationary solution to the hyperbolic NSK equations satisfies the system

$$\nabla P(\rho) = \gamma\eta\nabla\cdot\left(\nabla^2\eta\right), \qquad \gamma\nabla^2\eta = \frac{1}{\gamma\alpha}\left(\frac{\eta}{\rho}-1\right). \tag{45}$$

Written in this form, equations (45) exhibit very close resemblance to the ODE (44), in the sense that the same equilibrium between pressure and capillary effects is obtained, only with ρ substituted by η in the surface tension terms. In order to demonstrate numerical convergence of the numerical solutions of (45) to those of the original system (44), we seek here a non-constant equilibrium solution corresponding to a phase transition between two bulk states ρ_L and ρ_V denoting liquid and vapor densities, respectively. A possibility to obtain such an equilibrium is to solve numerically the following initial value problem

$$\begin{cases} \rho''' = \frac{1}{\gamma\rho}P'(\rho) \\ \rho_{x=0} = \rho_L, \\ \rho'_{x=0} = -\epsilon \\ \rho''_{x=0} = 0. \end{cases} \tag{46}$$

where $\rho_L = 1.80714032732$ and $\epsilon = 10^{-8}$ are prescribed. We use here a classical Runge-Kutta method of order four (RK4) to solve the ODE with a step size of $\Delta x = 10^{-4}$ and a surface tension coefficient $\gamma = 10^{-3}$. Note that the behavior of the solution is extremely sensitive to the precision of these values, as shown in Figure 4, where one can see that the number of digits taken in ρ_L drastically affects the shape of the numerical solution. The phase portrait shows in particular that the vapor state ρ_L is located at a saddle point which is particularly hard to reach by numerical integration.

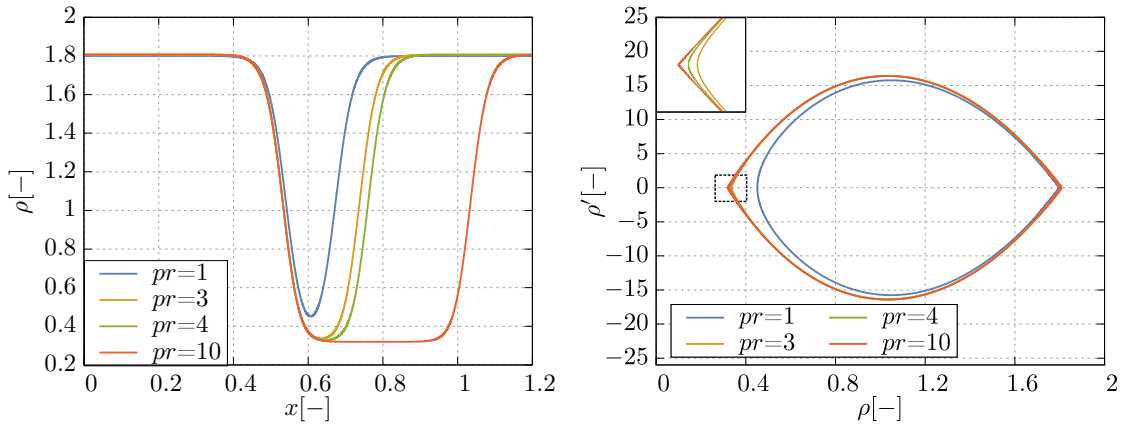

Figure 4: Influence of the precision pr of the initial value ρ_L on the behaivor of the solution $\rho(x)$ (left) and on the phase portrait (right) for a fixed value of $\epsilon = 10^{-8}$. The profiles are obtained numerically using a RK4 scheme with $dx = 10^{-4}$ and $\gamma = 10^{-3}$. the inset in the left figure corresponds to a zoom over the marked region around the angular point.

The same behavior is observed when solving the equivalent initial-value problem for our hyperbolic system which in one dimension of space is given by

$$\begin{cases} \rho' = \frac{p}{\frac{\eta}{\rho}+\frac{\alpha}{\eta}\rho P'(\rho)}, \\ \eta' = p, \\ p' = \frac{1}{\alpha\gamma\rho}(\rho-\eta), \\ \rho_{x=0} = \eta_{x=0} = \rho_L, \\ p_{x=0} = -\epsilon \end{cases} \tag{47}$$

The numerical solution to the latter, for several values of α is given in Figure 5 along the corresponding convergence Table 1. The variables ρ and p of the hyperbolic model are compared respectively with ρ and $\nabla\rho$ of the reference system. The table indicates a first-order convergence rate of the numerical solution in all of the L_2, L_1 and L_∞ norms.

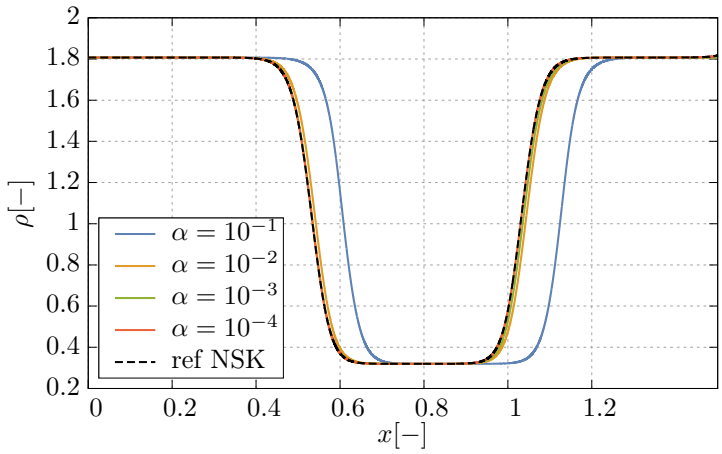

Figure 5: Comparison of the numerical 1-d static bubble solution of the initial-value problem (47) for different values of the penalty parameter α (continuous lines) with the reference solution of the NSK system (46) (black dashed line).

α	$\epsilon_{L_2}(\rho)$	$\epsilon_{L_1}(\rho)$	$\epsilon_{L_\infty}(\rho)$	$O_{L_2}(\rho)$	$O_{L_1}(\rho)$	$O_{L_\infty}(\rho)$
10^{-1}	2.83×10^{-1}	1.11×10^{-1}	1.04			
10^{-2}	3.24×10^{-2}	1.19×10^{-2}	1.30×10^{-1}	0.94	0.97	0.90
10^{-3}	3.23×10^{-3}	1.18×10^{-3}	1.29×10^{-2}	1.00	1.00	1.00
10^{-4}	3.26×10^{-4}	8.30×10^{-5}	9.06×10^{-4}	1.15	1.15	1.15
α	$\epsilon_{L_2}(p)$	$\epsilon_{L_1}(p)$	$\epsilon_{L_\infty}(p)$	$O_{L_2}(p)$	$O_{L_1}(p)$	$O_{L_\infty}(p)$
10^{-1}	4.54	2.01	14.76			
10^{-2}	6.35×10^{-1}	2.59×10^{-1}	2.29	0.85	0.88	0.80
10^{-3}	6.34×10^{-2}	2.59×10^{-2}	2.29×10^{-1}	1.00	1.00	0.99
10^{-4}	4.44×10^{-3}	1.81×10^{-3}	1.59×10^{-2}	1.15	1.15	1.15

Table 1: Convergence table of the numerical 1-d static bubble solution of the initial value problem (47) to that of the original NSK system. Convergence is shown in the penalty parameter α. The columns indicate respectively the values of α, the absolute error in the different norms ϵ_{L_2}, ϵ_{L_1} and ϵ_{L_∞} and their corresponding order of convergence respectively for the variables ρ then for p.

4.2. 1D travelling wave solutions

In order to obtain travelling wave solutions, we assume that every variable only depends on x and t by means of a single variable $\xi = x - st$. This allows to obtain solutions that are propagated in time with a constant speed s while maintaining their shape. Under this assumption, equation (1) reduces to the ODE

$$\begin{cases} \rho''' = \frac{1}{\gamma\rho}\left((P'(\rho) - (u-s)^2)\rho' - \frac{4}{3}\mu(u-s)\left(2\frac{\rho'^2}{\rho^2} - \frac{\rho''}{\rho}\right)\right) \\ u' = \frac{s-u}{\rho}\rho' \end{cases} \tag{48}$$

A thorough investigation of the behavior of the solutions as a function of γ, μ and s is out of the scope of this work. Nevertheless, the reader is referred to [2], where possible profiles of Riemann problem solutions for a simplified case are discussed, and to [37] for travelling wave solutions for the Navier-Stokes-Korteweg system. In any case, for a system where viscosity and dispersion are present, profiles that are periodic,

oscillatory or damped can be recovered by varying the viscosity μ, while keeping the remaining parameters constant. Profiles obtained in this way are represented in Figure 6, along the corresponding phase portraits, by taking for example the following initial condition

$$\rho_{x=0} = 1.8, \quad \rho'_{x=0} = -10^{-16}, \quad \rho''_{x=0} = 0, \quad u_{x=0} = 0 \tag{49}$$

and solving the corresponding initial-value problem by using a *RK4* scheme. The initial value of ρ', while small, is necessary to obtain a trivial constant state.

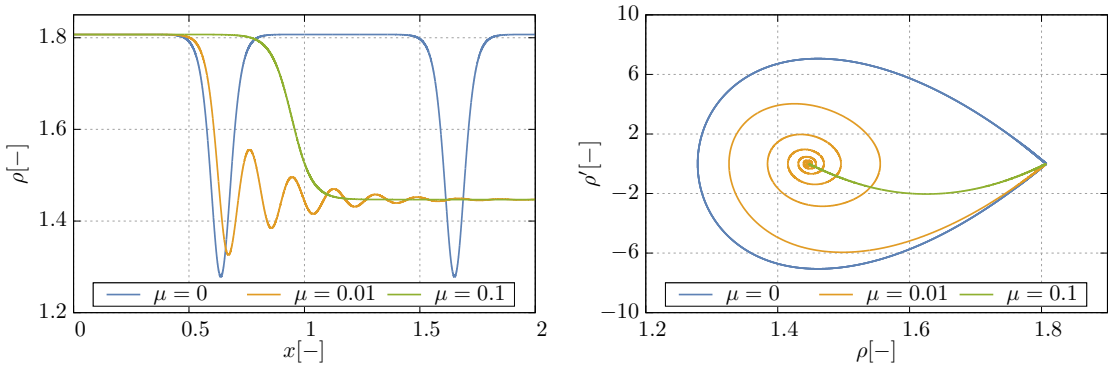

Figure 6: Numerical travelling wave profiles (left) and their corresponding phase portraits (right) for the Navier-Stokes-Korteweg system, for different values of μ, obtained by solving an initial-value problem using a *RK4* scheme. Other parameters used here are $\gamma = 0.001$, $s = 1$.

It is possible to compute equivalent solutions for our hyperbolic model. Alternatively, it seems interesting to see how well our system responds if an exact traveling wave solution to the original NSK equation is instead inserted as an initial condition. This will allow to verify how well a solution to the original NSK system can be considered an approximate solution to our model and if its main features can be recovered. For that we consider the following experiment. We take the exact solution to the IVP (48)-(49) and take it as an initial condition for the hyperbolic NSK system, solved numerically by a $\mathbb{P}_3\mathbb{P}_3$ discontinuous Galerkin method with a posteriori WENO limiting. The total computational domain is $\Omega = [0, 8]$, which is discretized on a uniform grid of $N_x = 512$ cells. The CFL number is set to 0.9. We assume the scaling (28) for the relaxation parameters and take several values of α with a fixed value for the capillary coefficient $\gamma = 10^{-3}$ and the wave speed $s = 1$. As for the viscosity, we recall here that the GPR model does not depend explicitly on μ but has rather an effective viscosity coefficient that is dependent on the relaxation characteristic time τ as well as the shear velocity c_s as well as a reference density ρ_0. Therefore, in all what follows, whenever we need to prescribe an effective viscosity coefficient, we shall impose the shear velocity c_s and adjust the timescale accordingly to recover the sought value of μ. In the following simulations for travelling wave solutions, the shear velocity will be taken as $c_s = 10$. The value of the reference density will be fixed to $\rho_0 = 1$ throughout the following experiments. Thus, for the travelling wave solutions we consider here, we consider two values of the effective velocities given by $\mu = 10^{-2}$ and $\mu = 10^{-1}$, and which correspond respectively to a damped wave and an oscillatory wave-train. The results, which are shown in Figures 7 and 8, show that there is a good agreement between the exact solution and the approximate solution for low values of the penalty parameter α. Perturbations in the solution become noticeable when α is fairly high for both chosen profiles. This experiment shows that for small enough α, travelling wave solutions to the original NSK system can be considered approximate travelling wave solutions to our new hyperbolic model.

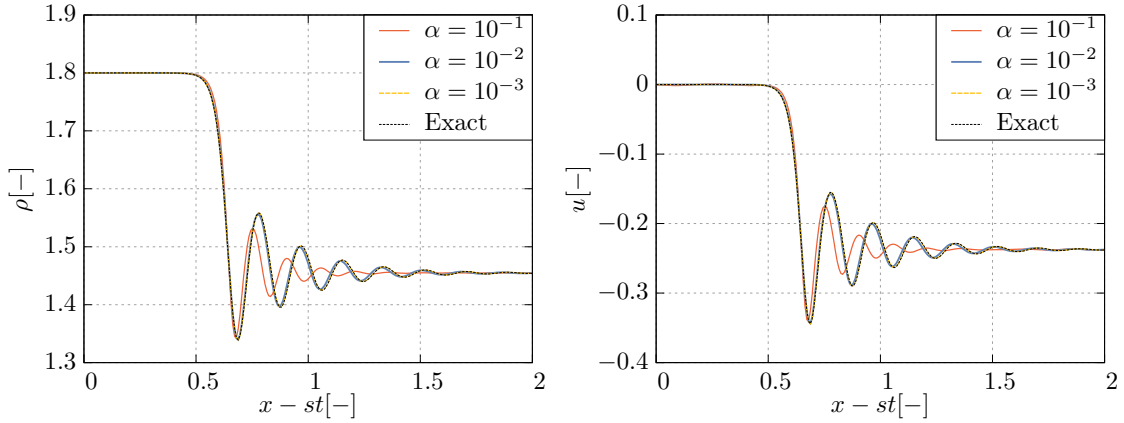

Figure 7: Numerical solution to the hyperbolic NSK system obtained by a $\mathbb{P}_3\mathbb{P}_3$ discontinuous Galerkin scheme, for an exact oscillatory travelling wave of the original NSK system for $\alpha = 10^{-1}, 10^{-2}, 10^{-3}$ and under the scaling (28). The surface tension coefficient is $\gamma = 10^{-3}$ and the effective viscosity coefficient is $\mu = 0.01$. The wave speed is $s = 1$. The total domain is $[0, 8]$, discretized over $N_x = 512$ cells. The solution is displayed at $t = 2$.

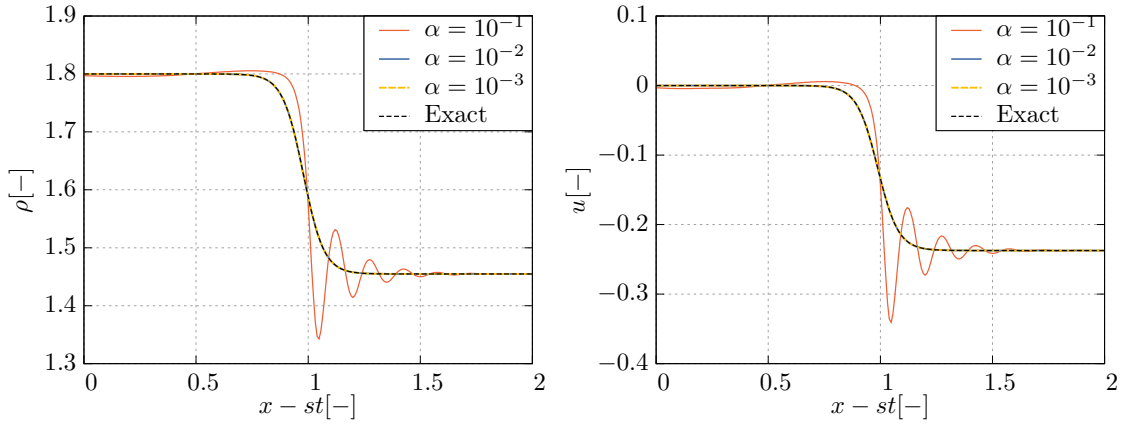

Figure 8: Numerical solution to the hyperbolic NSK system obtained by a $\mathbb{P}_3\mathbb{P}_3$ discontinuous Galerkin scheme, for an exact damped travelling wave of the original NSK system for $\alpha = 10^{-1}, 10^{-2}, 10^{-3}$ and under the scaling (28). The surface tension coefficient is $\gamma = 10^{-3}$ and the effective viscosity coefficient is $\mu = 0.1$. The wave speed is $s = 1$. The total domain is $[0, 8]$, discretized over $N_x = 512$ cells. The solution is displayed at $t = 2$.

However, since these solutions are not exact solutions to the HNSK model, a convergence table cannot be obtained, as the relaxation error would set the threshold. Therefore, we have also computed an exact travelling wave solution in the dissipationless case by computing the ODE for the HNSK model and which

writes

$$\rho' = f(\eta, \rho, u, p) \tag{50a}$$

$$u' = \frac{s-u}{\rho} f(\eta, \rho, u, p) \tag{50b}$$

$$\eta' = p \tag{50c}$$

$$p' = \frac{\frac{1-\eta/\rho}{\alpha} + \beta(u-s)^2 p f(\eta, \rho, u, p)}{\beta\rho(u-s)^2 - \gamma} \tag{50d}$$

$$\text{where} \quad f(\eta, \rho, u, p) = \frac{((2\eta-\rho)/\rho - \gamma((\rho-\eta)/\rho)/(\beta\rho(u-s)^2-\gamma))p}{\eta^2/\rho^2 + \alpha(P'(\rho) - (u-s)^2 + \gamma\beta(u-s)^2 p^2/(\beta\rho(u-s)^2-\gamma))}$$

Solving this ODE allows to obtain a reference travelling wave solution, for which we could draw the following convergence table.

Table 2: Numerical convergence table for the traveling wave solution (50) using an ADER-DG $\mathbb{P}_N\mathbb{P}_M$ schemes with a *A posteriori* WENO limiting in one dimension of space. N_x denotes the number of mesh points. The columns refer to the L_2 norms of the error with respect to the exact solution and their corresponding convergence order O_2 for indicative variables.

	N_x	$\epsilon_{L_2}(\rho)$	$\epsilon_{L_2}(u)$	$\epsilon_{L_2}(\eta)$	$\epsilon_{L_2}(w)$	$\epsilon_{L_2}(p)$	$O_{L_2}(\rho)$	$O_{L_2}(u)$	$O_{L_2}(\eta)$	$O_{L_2}(w)$	$O_{L_2}(p)$
$\mathbb{P}_2\mathbb{P}_2$											
	16	1.69×10^{-3}	5.98×10^{-3}	1.69×10^{-3}	2.78×10^{-1}	7.45×10^{-2}					
	32	6.44×10^{-4}	7.58×10^{-4}	6.38×10^{-4}	6.84×10^{-2}	3.61×10^{-2}	1.40	2.98	1.40	2.02	1.05
	64	1.24×10^{-4}	1.53×10^{-4}	1.22×10^{-4}	1.19×10^{-2}	4.87×10^{-3}	2.37	2.31	2.38	2.52	2.89
	128	1.57×10^{-5}	2.76×10^{-5}	1.54×10^{-5}	1.86×10^{-3}	3.88×10^{-4}	2.99	2.47	2.99	2.68	3.65
$\mathbb{P}_3\mathbb{P}_3$											
	16	1.73×10^{-3}	4.06×10^{-3}	1.72×10^{-3}	3.19×10^{-1}	8.50×10^{-2}					
	32	1.48×10^{-4}	4.53×10^{-4}	1.47×10^{-4}	3.17×10^{-2}	7.09×10^{-3}	3.54	3.16	3.55	3.33	3.58
	64	2.72×10^{-6}	8.89×10^{-6}	2.66×10^{-6}	4.52×10^{-4}	2.04×10^{-4}	5.77	5.67	5.79	6.13	5.12
	128	3.37×10^{-8}	4.16×10^{-7}	3.20×10^{-8}	8.71×10^{-6}	3.17×10^{-6}	6.33	4.42	6.38	5.70	6.00
$\mathbb{P}_4\mathbb{P}_4$											
	16	6.00×10^{-4}	1.82×10^{-3}	5.93×10^{-4}	1.59×10^{-1}	3.93×10^{-2}					
	32	5.76×10^{-6}	1.09×10^{-5}	5.59×10^{-6}	7.98×10^{-4}	4.32×10^{-4}	6.70	7.38	6.73	7.64	6.51
	64	3.53×10^{-7}	6.93×10^{-7}	3.43×10^{-7}	4.48×10^{-5}	1.79×10^{-5}	4.03	3.98	4.03	4.16	4.60
	128	1.12×10^{-8}	3.35×10^{-8}	1.10×10^{-8}	1.26×10^{-6}	3.70×10^{-7}	4.97	4.37	4.96	5.15	5.59
$\mathbb{P}_5\mathbb{P}_5$											
	5	1.14×10^{-2}	1.87×10^{-2}	1.87×10^{-2}	1.08×10^{-0}	4.38×10^{-1}					
	10	1.59×10^{-3}	5.87×10^{-3}	1.57×10^{-3}	5.20×10^{-1}	1.25×10^{-1}	2.84	1.67	3.57	1.06	1.81
	20	3.60×10^{-5}	8.36×10^{-5}	3.55×10^{-5}	8.32×10^{-3}	1.94×10^{-3}	5.47	6.13	5.47	5.97	6.01
	40	6.26×10^{-7}	1.88×10^{-6}	6.18×10^{-7}	1.33×10^{-4}	2.64×10^{-5}	5.85	5.47	5.84	5.97	6.20

4.3. 2D stationary bubble

In multiple dimensions of space, static solutions of interest generally display radial symmetry. Thus, it would be more convenient to consider an appropriate system of coordinates in this case which are polar coordinates for $d = 2$ and spherical coordinates for $d = 3$. Under these assumptions, the ODE (44) for the static NSK system can be cast into the form

$$\frac{\partial\rho}{\partial r^3} + \frac{d-1}{r}\frac{\partial\rho}{\partial r^2} - \left(\frac{d-1}{r} + \frac{1}{\gamma\rho}P'(\rho)\right) = 0 \tag{51}$$

to which corresponds the following ODE for our hyperbolic model, written in polar coordinates as

$$\rho' = \frac{p}{\frac{\eta}{\rho} + \frac{\alpha}{\eta}\rho P'(\rho)}, \qquad \eta' = p, \qquad p' = -\frac{d-1}{r}p - \frac{1}{\alpha\gamma\rho}(\rho - \eta). \tag{52}$$

Similarly to the 1D case, we are seeking non-constant equilibrium solutions and we consider an initial-value problem with the following possible initial conditions, corresponding to a droplet or a bubble at rest,

respectively

$$\begin{cases} \text{Droplet:} & \rho_{r=0} = 1.823, \quad \eta_{r=0} = \rho + \epsilon_1, \quad p_{r=0} = 0, \\ \text{Bubble:} & \rho_{r=0} = 0.310, \quad \eta_{r=0} = \rho + \epsilon_2, \quad p_{r=0} = 0, \end{cases} \tag{53}$$

where $\epsilon_1 = -9.05876663682 \times 10^{-8}$ and $\epsilon_2 = 1.69493835634 \times 10^{-10}$ are necessary perturbations in order not to obtain a constant equilibrium solution. Once again, the solution is highly sensitive to the accuracy of these perturbations. The values of the initial densities are taken in the vicinity of the Maxwell states ρ_L^M and ρ_V^M for the liquid and vapor phase, respectively. The density in the surrounding state, farther from the center, is determined such that the chemical potential is the same in both phases. Solving the ODE for $r \in [0, R]$ allows to obtain the radial profiles of Figure 9. These solutions are then used as an initial condition for our ADER-DG code. In our case, we use $R = 0.7$. However, the total domain used for the 2D simulation is $[-1, 1] \times [-1, 1]$ which extends further than the provided radial solution. Therefore, in this case, and for $\sqrt{x^2 + y^2} > R$, the initial condition is continued with a constant state matching the values at $r = R$, except for $\mathbf{p}$ which is taken identically null. For this test, we use a Cartesian mesh of 144×144 cells and the values of the parameters are $\gamma = 10^{-3}$, $\mu = 10^{-2}$, $c_s = 10$, $\alpha = 10^{-2}$, $\beta = 10^{-3}$ and $b_c = 500$. The final time is $t = 10$. The results are shown in Figure 10 and along a radial cut in Figure 11.

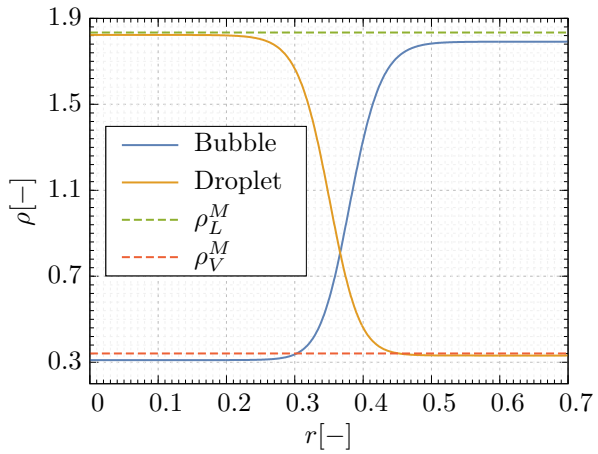

Figure 9: ODE solution of equation (52) in polar coordinates for $d = 2$ with the initial conditions (53) and a Van der Waals pressure law (6)-(7). The dashed lines represent the Maxwell states ρ_L^M and ρ_V^M. The penalty parameter is taken equal to $\alpha = 10^{-2}$.

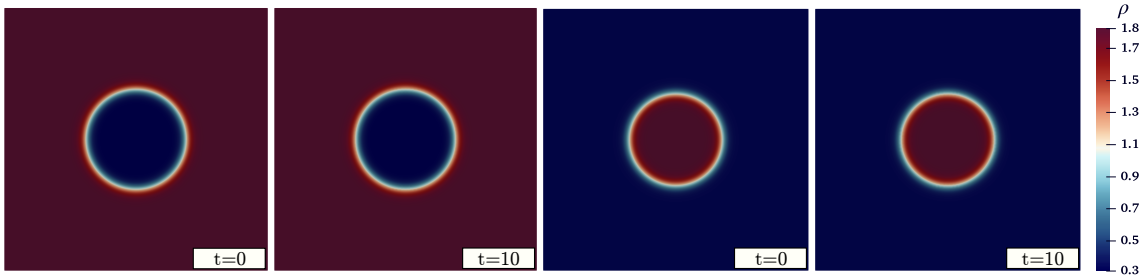

Figure 10: Numerical results of the hyperbolic NSK system obtained by an ADER-DG $\mathbb{P}_3\mathbb{P}_3$ scheme with *a posteriori* WENO limiting, for the reference stationary solutions displayed in Figure 9. The total computational domain is $[-1, 1] \times [-1, 1]$ discretized over a Cartesian mesh of 144×144 cells. Parameters used here are $\gamma = 10^{-3}$, $\mu = 10^{-2}$, $c_s = 10$, $\alpha = 10^{-2}$, $\beta = 10^{-3}$ and $b_c = 500$. The solution is displayed at $t = 10$.

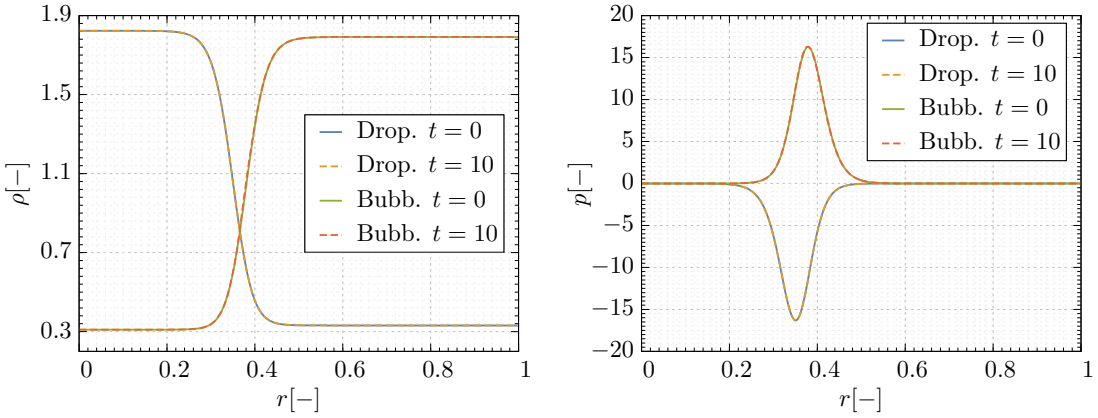

Figure 11: Radial cut of the stationary numerical solutions of Figure 10, at $t = 10$ compared with their respective initial conditions for both ρ (left) and $\mathbf{p}$ (right).

4.4. 2D stationary bubble: Mesh convergence analysis

In the previous section we extrapolated the initial condition to a bigger computational domain with a constant state. While the results are stable and satisfactory, the error induced by the extrapolation puts a threshold to the numerical error and which cannot be overlooked in a mesh convergence analysis. An alternative solution is to use an initial condition provided by a boundary-value solver instead of a Cauchy problem. This allows to obtain more accurate benchmarking solutions. For what follows, the numerical resolution of the boundary value problems is done by using the COLNEW BVP solver [4, 5, 7], which was also used in [37]. In order to verify whether the provided solutions are also coherent with the original Navier-Stokes-Korteweg system, two different boundary value problems are solved, for the ODEs (51) and (52), for which the boundary values are given respectively as follows

$$\text{(NSK):} \begin{cases} \rho(r=0) = 1.825 \\ \rho'(r=0) = 0 \\ \rho(r=1) = 0.33282591 \end{cases}, \quad \text{(HNSK):} \begin{cases} \rho_{r=0} = 1.825 \\ p(r=0) = 0 \\ p(r=1) = 0. \end{cases} \tag{54}$$

The initial guess for ρ is given in the following form

$$\rho(r) = \rho_v + \frac{\rho_l - \rho_v}{2}\text{erfc}((r-R)/\epsilon) \tag{55}$$

where $\rho_l = 1.825$, $\rho_v = 0.34$, $R = 0.302$ and $\epsilon = 0.05$. The remaining variables for the HNSK are initialized as $\eta = \rho$ and $p = \eta'$. Solving these BVPs for both the NSK and the HNSK system for different values of α and for $\gamma = 10^{-3}$ yields the following results

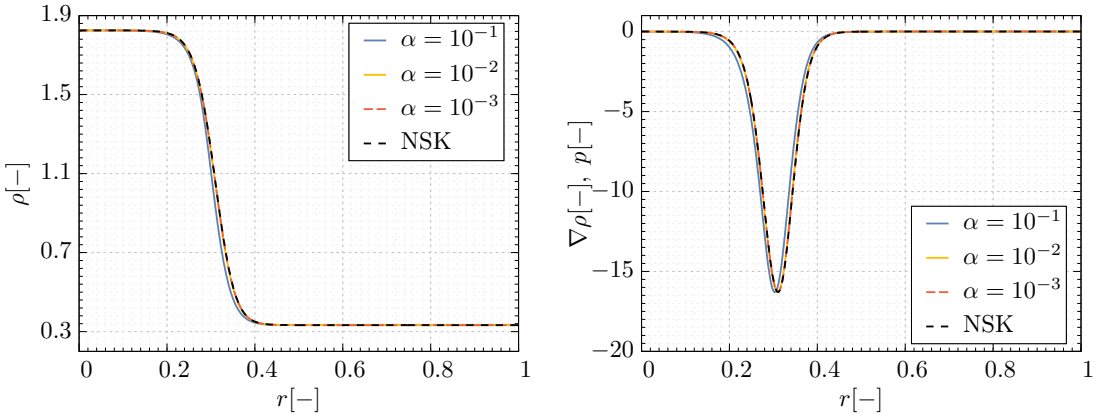

Figure 12: Boundary value problem solution for both NSK system and the HNSK system. The left figure shows the radial density profile while the right one shows p for the HNSK compared with ρ' for the NSK system. Different values of α are used and the surface tension coefficient is taken as $\gamma = 10^{-3}$.

Figure 12 shows a good agreement between the original model and our hyperbolic approximation. Lower values of the penalty parameter α show a better accuracy, as expected. We then take the solution for $\alpha = 10^{-3}$ and use it as an initial condition into our ADER-DG code and the numerical error is reported for different mesh resolutions as well as different orders of the numerical method. The results are summarized in Table 3. In the scope of this mesh convergence analysis, the limiter is disabled in order to speed up computations. The parameters used for this test are $\gamma = 10^{-3}$, $\alpha = 10^{-}3$, $\beta = 10^{-3}$, $c_s = 0$, $b_c = 10$. The final time is $t = 0.025$.

Table 3: Numerical convergence table for a stationary bubble solution , using ADER-DG $\mathbb{P}_N\mathbb{P}_N$ schemes in two dimensions of space. The mesh is comprised of $N_x \times N_y$ cells where N_x is indicated and $N_y = N_x$. The columns refer to the L_2 norms of the error with respect to the exact solution and their corresponding convergence order O_2 for indicative variables.

	N_x	$\epsilon_{L_2}(\rho)$	$\epsilon_{L_2}(u)$	$\epsilon_{L_2}(\eta)$	$\epsilon_{L_2}(w)$	$\epsilon_{L_2}(p)$	$O_{L_2}(\rho)$	$O_{L_2}(u)$	$O_{L_2}(\eta)$	$O_{L_2}(w)$	$O_{L_2}(p)$
$\mathbb{P}_2\mathbb{P}_2$											
	50	9.12×10^{-4}	6.63×10^{-2}	1.32×10^{-3}	2.00×10^{-0}	1.22×10^{-1}					
	75	5.05×10^{-4}	2.45×10^{-2}	5.86×10^{-4}	1.17×10^{-0}	2.86×10^{-2}	1.46	2.46	2.00	1.34	3.57
	100	3.09×10^{-4}	1.06×10^{-2}	3.26×10^{-4}	6.31×10^{-1}	2.60×10^{-2}	1.70	2.90	2.03	2.13	0.33
	200	5.08×10^{-5}	1.26×10^{-3}	5.19×10^{-5}	7.30×10^{-2}	6.77×10^{-3}	2.61	3.07	2.65	3.11	1.94
$\mathbb{P}_3\mathbb{P}_3$											
	50	2.06×10^{-4}	8.60×10^{-3}	2.29×10^{-4}	4.84×10^{-1}	1.59×10^{-2}					
	75	6.30×10^{-5}	1.59×10^{-3}	6.26×10^{-5}	1.29×10^{-1}	9.17×10^{-3}	2.92	4.17	3.19	3.26	1.35
	100	2.04×10^{-5}	4.03×10^{-4}	1.96×10^{-5}	3.80×10^{-2}	4.26×10^{-3}	3.92	4.76	4.04	4.24	2.67
	125	7.12×10^{-6}	1.47×10^{-4}	6.89×10^{-6}	1.16×10^{-2}	1.92×10^{-3}	4.71	4.53	4.68	5.31	3.57
$\mathbb{P}_4\mathbb{P}_4$											
	50	5.99×10^{-5}	1.20×10^{-3}	5.60×10^{-5}	1.43×10^{-1}	1.15×10^{-2}					
	100	2.68×10^{-6}	3.56×10^{-5}	2.54×10^{-6}	3.45×10^{-3}	7.24×10^{-4}	4.48	5.08	4.46	5.37	4.00
	125	9.47×10^{-7}	1.19×10^{-5}	8.90×10^{-7}	1.02×10^{-3}	2.65×10^{-4}	4.66	4.90	4.70	5.48	4.50
	150	3.82×10^{-7}	4.83×10^{-6}	3.66×10^{-7}	3.47×10^{-4}	1.06×10^{-4}	4.97	4.96	4.87	5.90	5.02
$\mathbb{P}_5\mathbb{P}_5$											
	25	4.11×10^{-4}	1.17×10^{-2}	4.06×10^{-4}	1.15×10^{-0}	6.67×10^{-2}					
	50	6.62×10^{-6}	1.15×10^{-4}	6.37×10^{-6}	1.25×10^{-2}	1.52×10^{-3}	5.96	6.66	5.99	6.53	5.46
	75	8.48×10^{-7}	1.15×10^{-5}	8.39×10^{-7}	9.73×10^{-4}	2.06×10^{-4}	5.07	5.68	5.00	6.30	4.93
	100	1.46×10^{-7}	1.88×10^{-6}	1.41×10^{-7}	1.25×10^{-4}	4.54×10^{-5}	6.11	6.29	6.19	7.13	5.25

4.5. Ostwald ripening

4.5.1. One dimensional case

In this part, we are considering a dynamical case. Consider an initial condition where several vapor regions, to which we can refer to as bubbles, are surrounded by a liquid phase. In the setting of the Navier-Stokes-Korteweg model, precisely due to the gradient term, this configuration will evolve towards a single

bubble, in an attempt to minimize the density gradients and thus reach an energetically more stable profile for the same mass. If the bubbles are not in the close vicinity of one another, the process by which they combine is not coalescence. Instead, smaller bubbles shrink and release their 'mass' throughout the medium and which is then gradually absorbed by larger bubbles. The process continues until only one bubble remains. This is called Ostwald ripening and was also studied in [29, 59]. We consider the following initial condition for ρ and u

$$\rho(x,0) = \rho_l + \frac{\rho_l - \rho_v}{2} \sum_{k=1}^{n_b} \left(\tanh\left(\frac{x - x_k - r_k}{\epsilon} \right) - \tanh\left(\frac{x - x_k + r_k}{\epsilon} \right) \right), \quad u(x,0) = 0 \tag{56}$$

where $\rho_l = 1.8$, $\rho_v = 0.3$ represent the liquid density and vapor density, respectively, n_b is the number of bubbles, each of which is defined by a center position x_k and a radius r_k and ϵ is a parameter that controls the initial thickness of the transition region. The final state only depends on the intrinsic properties of the system and mainly on the surface tension coefficient γ. We consider two bubbles at the positions $x_1 = 0.75$, $x_2 = 1.25$ with radii $r_1 = 0.15$ and $r_2 = 0.05$, respectively. The total domain $\Omega = [0, 2]$ is discretized via $N_x = 200$ cells. The surface tension coefficient is $\gamma = 10^{-3}$, the effective GPR viscosity is $\mu = 10^{-2}$ with a shear velocity of $c_s = 10$. The relaxation parameters are $\alpha = 10^{-2}$ and $\beta = 10^{-5}$. The CFL number is set to 0.9. The numerical solution obtained by an ADER-DG $\mathbb{P}_3\mathbb{P}_3$ scheme with *a posteriori* WENO limiting is given in Figure 13 at different times.

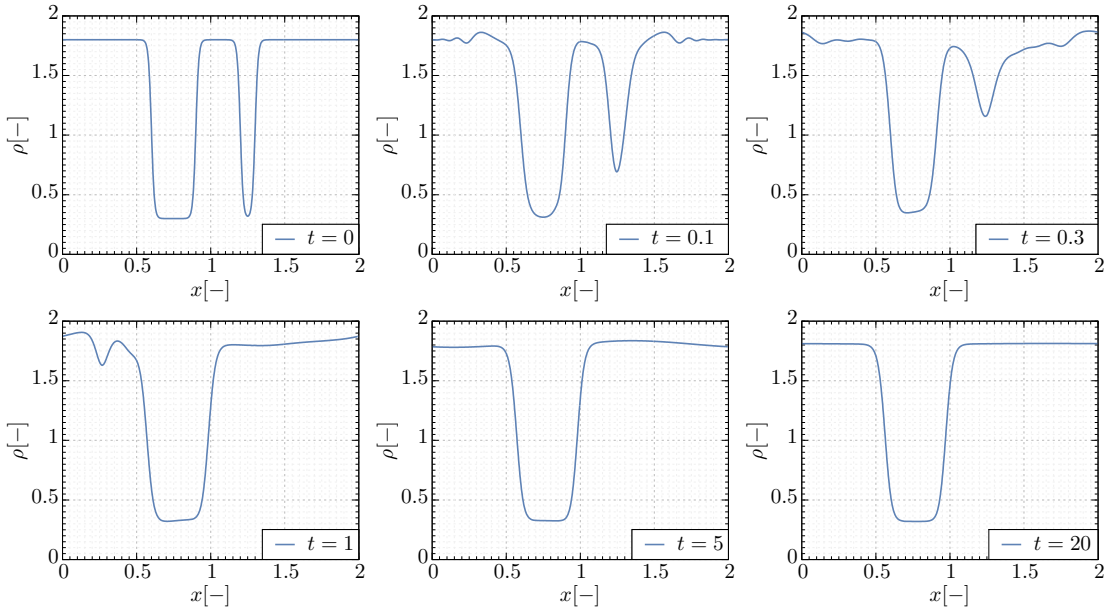

Figure 13: Density profile for the 1D Ostwald ripening simulation plotted at six different times $t \in \{0, 0.1, 0.3, 1, 5, 20\}$ obtained by an ADER-DG $\mathbb{P}_3\mathbb{P}_3$ scheme with *a posteriori* WENO limiting. Parameters used for this simulation are $\gamma = 10^{-3}$, $\mu = 10^{-2}$, $c_s = 10$, $\alpha = 10^{-2}$ and $\beta = 10^{-5}$. The domain is discretized over $N_x = 200$ cells.

The boundary conditions used for this simulation are periodic. In order to re-verify that convergence in both the mesh and in the relaxation parameters persist for a solution that exhibits more complex dynamics, Figure 14 shows a comparison of our results with two other numerical solutions, one obtained for a finer grid ($N_x = 1024$)and the other for stiffer relaxation parameters ($\alpha = 10^{-3}$, $\beta = 10^{-6}$). The comparison is done at instants close to the vanishing of the small bubble, since more density and velocity fluctuations are observed around these instants. The figure shows good convergence properties in the sense that differences

are hardly discernible between the three curves, showing that the time scale and the dynamics are well-established and not very sensitive to the choice of parameters. Finally, in Figure 15 we plot the evolution of the total kinetic energy to show that the latter is decaying over time, as it should be in a dissipative system, and that the presented numerical solution is evolving towards a stationary state.

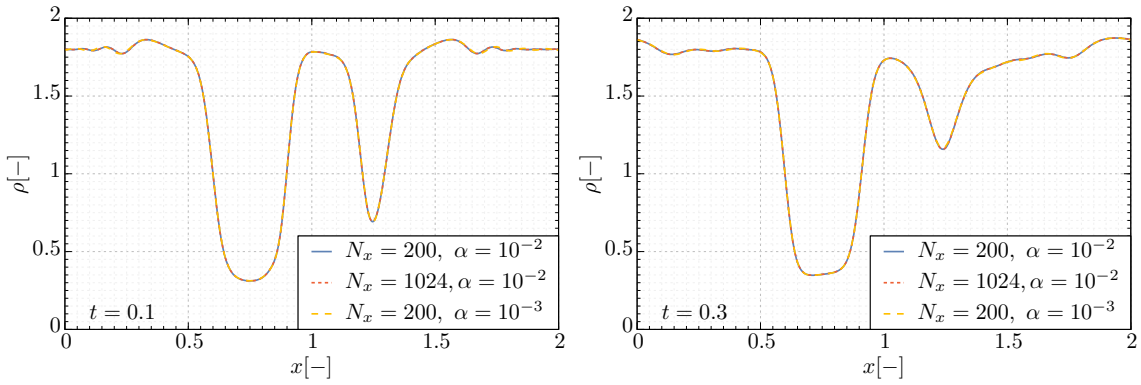

Figure 14: Comparison of our numerical result (blue continuous line) with two reference solutions, one corresponding to a finer grid of $N_x = 1024$ cells (red dashed line) while the other corresponds to the same mesh but stiffer relaxation parameters $\alpha = 10^{-3}$,$\beta = 10^{-6}$.

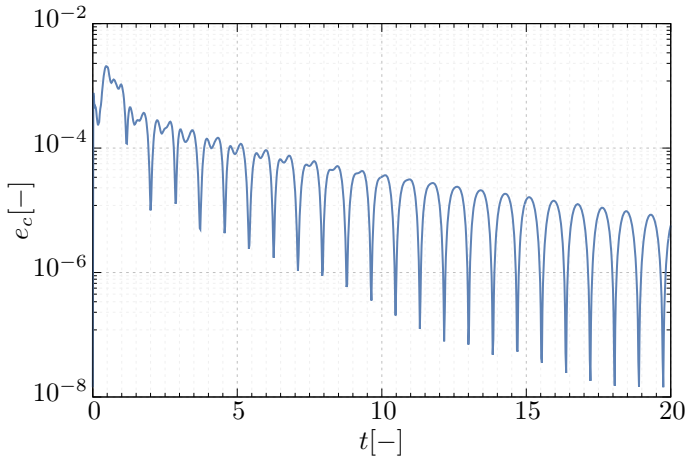

Figure 15: Time evolution of the kinetic energy over time for the Ostwald ripening test case in 1D.

4.5.2. Two-dimensional case

Ostwald ripening in two or higher dimensions follows the same principles as the one dimensional counterpart. However, compared to the latter, an additional complexity to be aware of is the non-violation of curl-involution constraints, for which the GLM curl-cleaning procedure is specifically implemented through equations (12). For this test case we consider an initial condition with a number of bubbles $n_b = 20$, which is prescribed in Cartesian coordinates as follows

$$\rho(x,0) = \rho_l + \frac{\rho_l - \rho_v}{2} \sum_{k=1}^{n_b} \left(\tanh\left(\frac{c_k - r_k}{\epsilon}\right) - \tanh\left(\frac{c_k + r_k}{\epsilon}\right)\right), \quad u(x,0) = 0, \tag{57}$$

where $c_k = \sqrt{(x - x_k)^2 + (y - y_k)^2}$ can seen as the radius in polar coordinates, defined locally for each bubble with their center (x_k, y_k) as the pole, r_k is the approximate radius of the bubble k and ϵ controls

the thickness of the transition region. The value of ϵ affects the dynamics of the bubbles. In particular, if it is higher (resp. lower) than the equilibrium value, this will initiate mass transfer in the vicinity of bubbles interfaces, in order to sharpen (reps. thicken) the latter, generating unnecessary perturbations in the medium. A good estimate was provided in [59] where they take $\epsilon = 2\sqrt{\gamma}$ and which we will consider for our simulations. We consider a computational domain of $[-1.1, 1.1]\times[-1.1, 1.1]$, discretized over 216×216 cells. The positions and radii for the initial bubbles are given in the following Table 4

k	1	2	3	4	5	6	7	8	9	10
r_k	0.20	0.15	0.10	0.10	0.10	0.10	0.10	0.10	0.10	0.10
x_k	0.00	0.60	−0.75	−0.70	−0.40	−0.20	0.00	0.40	0.60	0.80
y_k	0.00	0.60	0.00	0.60	−0.40	−0.80	0.60	−0.40	0.00	−0.40
k	11	12	13	14	15	16	17	18	19	20
r_k	0.05	0.05	0.05	0.05	0.05	0.05	0.05	0.05	0.05	0.05
x_k	−0.80	−0.70	−0.50	−0.40	−0.40	0.35	−0.10	0.15	0.40	0.70
y_k	−0.80	−0.50	−0.70	0.20	0.80	0.30	−0.45	−0.55	−0.80	−0.70

Table 4: Radii and positions of the bubbles used for the initial condition (58) displayed in Figure 16.

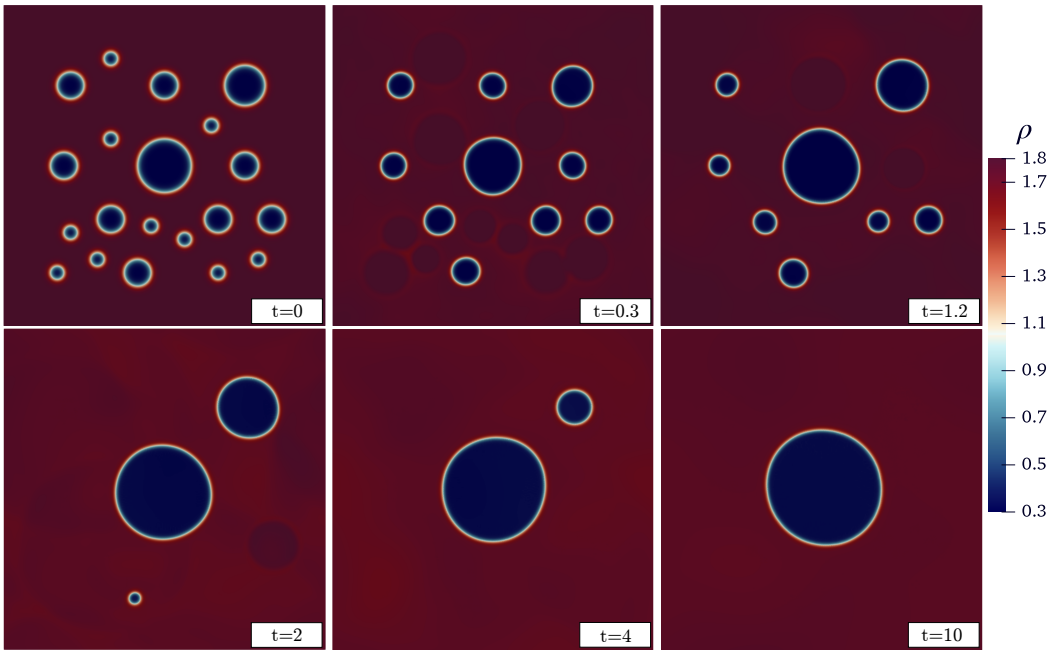

Figure 16: Numerical result for the density ρ, obtained by a $\mathbb{P}_3\mathbb{P}_3$ scheme with *a posteriori* WENO limiting, for the Ostwald ripening test case in two dimensions, plotted at several times $t \in \{0, 0.3, 1.2, 2, 4, 10\}$. Values used here are $\rho_l = 1.8$, $\rho_v = 0.3$, $\gamma = 2.10^{-4}$, $\alpha = 10^{-2}$, $\beta = 10^{-5}$, $c_s = 10$ and an effective viscosity of $\mu = 10^{-2}$. The cleaning parameter is taken as $b_c = 1200$. The total domain is $\Omega = [-1.2, 1.2] \times [-1.2, 1.2]$ discretized over a 288×288 uniform grid. Boundary conditions are periodic.

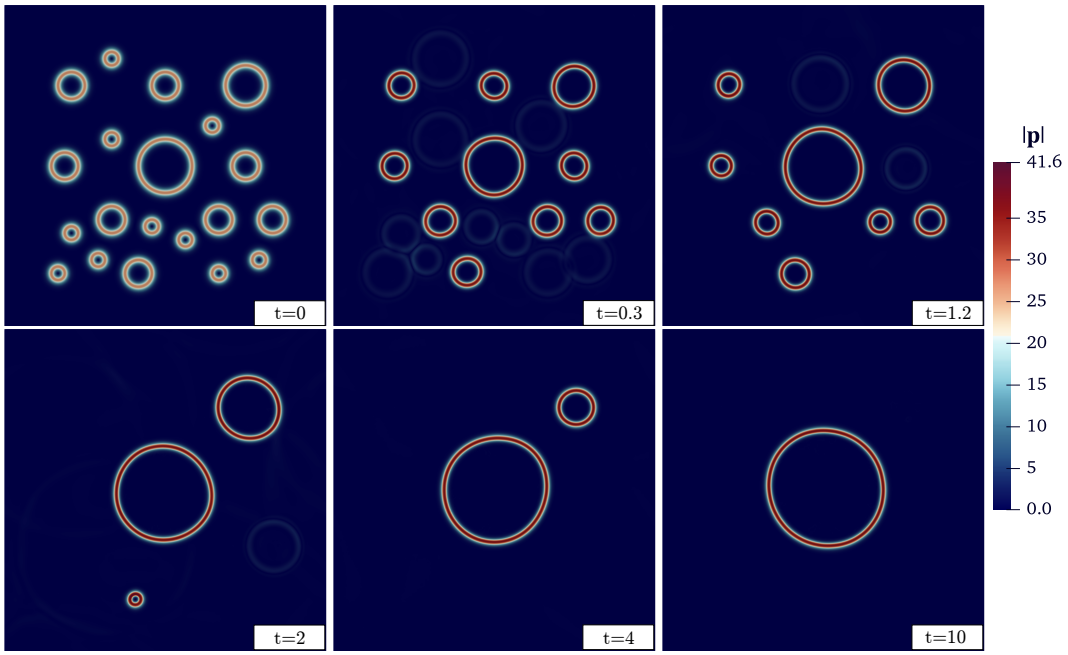

Figure 17: Numerical result for the magnitude of the gradient field **p** obtained in the same setting as the upper figure.

We take for this simulation initial densities in the vicinity of the Maxwell states $\rho_l = 1.8$ and $\rho_v = 0.3$. As for the model parameters, we use $\gamma = 2.10^{-4}$, $\alpha = 10^{-2}$, $\beta = 10^{-5}$, $c_s = 10$ and an effective viscosity of $\mu = 10^{-2}$. The numerical result is plotted in Figures 16 and 17. The observed dynamics corresponds qualitatively with what was observed previously in [37, 29, 59].

4.6. Cleaning analysis

4.6.1. Simplified testcase: Condensing bubble

In order to asses whether the GLM curl cleaning is contributing to the stability of the numerical solution, a few tests have been run in order to quantify how curl errors are affected by the choice of the cleaning parameter b_c. We consider a simplified test case where a single bubble is taken in a medium, large enough for it to completely condensate, so that only one phase remains at equilibrium. The expression of the initial bubble is given in the same fashion as in (58) by

$$\rho(x,0) = \rho_l + \frac{\rho_l - \rho_v}{2}\left(\tanh\left(\frac{r - r_0}{\epsilon}\right) - \tanh\left(\frac{r + r_0}{\epsilon}\right)\right), \quad u(x,0) = 0. \tag{58}$$

where the radius $r_0 = 0.10$ and the interface thickness $\epsilon = 2\sqrt{\gamma}$ are initially prescribed. We take for this simulation the values of $\rho_l = 1.8$ and $\rho_r = 0.3$, $\gamma = 5.10^{-4}$, $\alpha = 10^{-2}$, $\beta = 10^{-5}$, $c_s = 10$ and different values of the cleaning velocity, shown in Figure 19. The computational domain is taken as $\Omega = [-0.5, 0.5] \times [-0.5, 0.5]$ discretized over 64×64 cells. The typical timeline of the solution is plotted in Figure 18 for $b_c = 100$. Regardless of the chosen values, the dynamics of the solution are preserved, and differences in the density plot are of indiscernible magnitude.

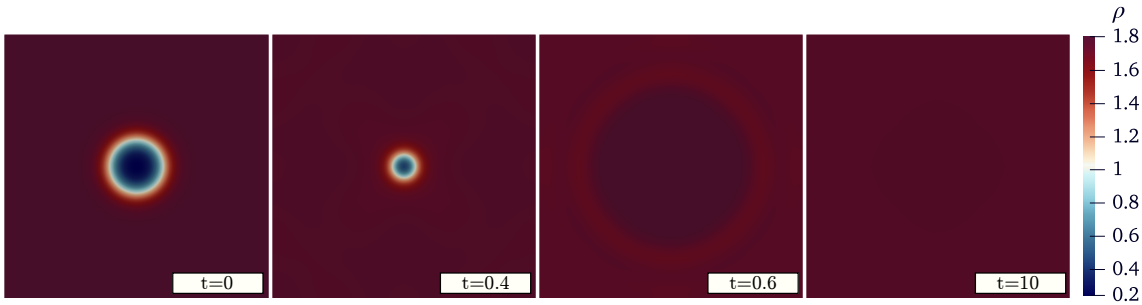

Figure 18: Plot of the numerical solution obtained for the initial condition (58) with the above mentioned parameters. The result is shown for $b_c = 100$.

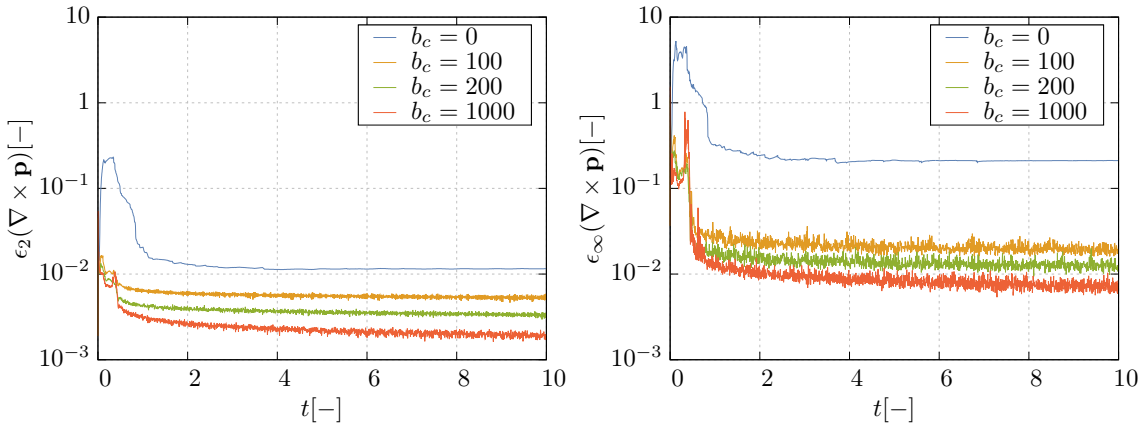

Figure 19: Normalized L_2 (left) and L_∞ norms of the curl errors across the computational domain.

For this test, we plot the L_2 and L_∞ errors of $\nabla \times \mathbf{p}$, normalized with respect to the magnitude of $\partial p_1/\partial x$ at time $t = 0$. The time evolution of these errors over time are reported in Figure 19. For this very simple test, where the gradient field is of negligible magnitude in the long term, the GLM curl cleaning procedure is in accordance with the expected result that curl errors are a decreasing function of the cleaning speed.

4.6.2. Non-condensing bubble

We consider now a similar initial condition to the previous one, where again a single bubble is taken in the center of a square domain, but the domain is taken small enough to keep a two-phase configuration. The main issue at hand in this test case respectively to the former is that high gradients of the density are present at all times during the simulation. In order to further highlight this complication, a slightly sharper interface will be considered as well, which is naturally be more prone to generating curl errors. For this simulation we take a slightly larger bubble with $r = 10$, $\rho_l = 1.8$ and $\rho_r = 0.3$, $\gamma = 2.10^{-4}$, $\alpha = 10^{-2}$, $\beta = 10^{-5}$, $c_s = 10$ and different values of the cleaning velocity, shown on figure 19. The total domain is taken as $\Omega = [-0.25, 0.25] \times [-0.25, 0.25]$ and is discretized over 128×128 cells. Compared, to the previous test case, a mesh refinement is necessary as sharper gradients are present in the solutions at all times and which need to be well-resolved. Since the initial solution is not an exact stationary state, a decaying oscillation of the bubble will be observed, until a stationary state is reached. As can be seen from the time evolution of the curl errors, patterns emerge showing that curl errors gradually grow and then suddenly decay at almost regular intervals in the first instants. Understanding these dynamics requires to investigate the dynamics of the cleaning field ψ, whose growth is only fueled by the curl errors, as can be understood from equation

(12). To that end, we show in Figure 21 a sequence of the numerical results for the magnitude of ψ_3, for several times taken in the vicinity of the first spike in the L_2 error. The times at which these results are taken, are marked in Figure 20.

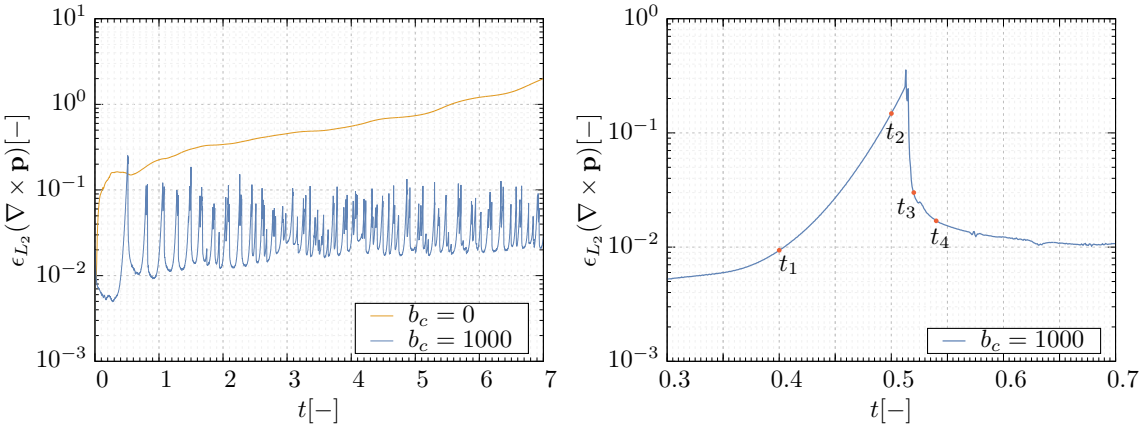

Figure 20: Left: Comparison of the time evolution of the normalized L_2 curl errors for two simulations with cleaning (blue line) and without cleaning (orange line). Right: A zoom on the first spike in the curl error. The marked dots correspond to times at which the cleaning field is displayed in figure 22.

The numerical experiment shows that the use of GLM curl-cleaning allows to significantly reduce the curl error and keep it from rising over time. As can be seen in Figure 20, in the absence of cleaning, curl errors show a continuously growing tendency, while under cleaning, the error keeps oscillating around the same order of magnitude. We presume that the oscillatory behavior is due to the dynamics of the curl cleaning field ψ, which transports curl errors away in a Maxwell-type subsystem. The dynamics of the curl cleaning field are shown in Figure 21. The times at which the cleaning field is displayed correspond to the marked times in right part of Figure 20. One can see that curl errors accumulate in specific regions, which actually correspond to the high-gradient transition separating both phases. Then, *cleaning waves* are emitted from these regions and which spread the error over the domain, thus preventing further concentration of the latter.

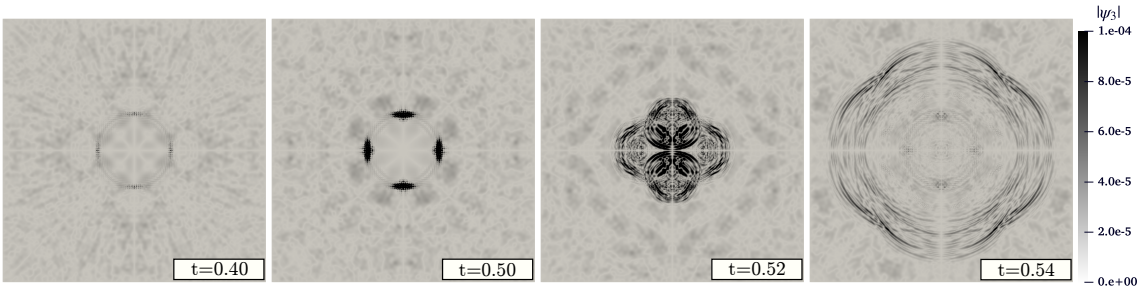

Figure 21: Behavior of the magnitude of the cleaning field component ψ_3 when accumulation of curl errors occurs.

4.6.3. Ostwald ripening

In a similar test case as the one presented in paragraph 4.5.2, we consider here a comparison for the Ostwald ripening case, where less symmetry and more complicated dynamics are at work. We take the same initial condition (58), with the values $\rho_l = 1.8$, $\rho_v = 0.3$, $\gamma = 5.10^{-4}$, $\alpha = 10^{-2}$, $\beta = 10^{-5}$, $c_s = 10$ and an effective viscosity of $\mu = 10^{-2}$. Since we compare here two simulations with and without curl

cleaning, the cleaning parameter is set as $b_c = 500$ for the former and b_c for the latter. The total domain is $\Omega = [-1.2, 1.2] \times [-1.2, 1.2]$ discretized over a 216×216 uniform grid. Boundary conditions are periodic. The time evolution for the normalized L_2 and L_∞ norms of the curl errors is reported on figure 22.

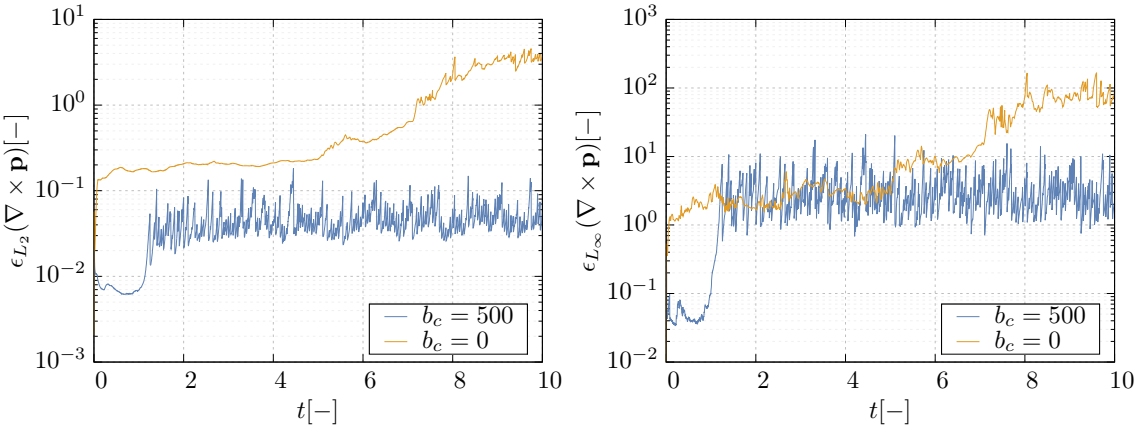

Figure 22: Comparison of the time evolution of the curl errors for two simulations with cleaning (blue line) and without cleaning (orange line).

Similarly to the previous test cases, the curl error are of smaller scale when the curl cleaning is present, and are kept at the same order of magnitude in the long term in contrast to the cleaning-less simulation where errors continue to increase. The behavior of the curl errors when cleaning is present is also more chaotic than in the previous tests, since the initial condition does not present any particular symmetries and the overall dynamics are considerably more complex.

5. Conclusion

In this paper, a new first-order hyperbolic relaxation model for the Navier-Stokes-Korteweg equations has been presented and has been solved numerically at the aid of high order ADER discontinuous Galerkin finite element schemes with *a posteriori* subcell finite volume limiter. The new model is based on a combination of the Godunov-Peshkov-Romenski model of continuum mechanics [70, 68, 48] and the extended Lagrangian approach for nonlinear dispersive systems forwarded in [55, 35]. The model was shown to reproduce the main features of the original NSK system at both the theoretical and practical level. In particular, a linearized dispersion analysis allowed us to show that our model reproduces very well the phase velocities and decay rates of the original NSK system for bounded wavelengths. Numerical solutions were shown to converge in both the the relaxation limit and the mesh size and exact solutions to the NSK system were shown to stable approximate solutions in our reformulation. There are many aspects which can still be addressed in the setting of the provided model and which are left for future endeavors. First, it seems interesting to substitute the GLM curl cleaning procedure used in this paper by using a family of exactly curl-free schemes [14] that would reduce the curl errors to machine zero. It seems of interest to further inspect the effectiveness of the curl-cleaning procedure and to compare it with exactly structure-preserving schemes. Another interesting line of investigation will be the development of efficient semi-implicit schemes [43, 54, 23, 11, 1, 38, 13, 73] in order to be able to address the low Mach number limit of the equations, in which the maximum characteristic speed goes to infinity, thus making explicit time-stepping highly inefficient and inaccurate. Future work will also concern the development of provably thermodynamically compatible schemes for the new model presented in this paper, similar to those recently forwarded in [21, 22, 19]. Finally, in order to properly address the sharp interface limit $\gamma \to 0$, it seems necessary to investigate whether suitable asymptotic-preserving schemes can be developed.

Acknowledgments

F.D. and M.D. are members of the INdAM GNCS group. The authors acknowledge the financial support received from the Italian Ministry of Education, University and Research (MIUR) in the frame of the Departments of Excellence Initiative 2018–2022 attributed to DICAM of the University of Trento (grant L. 232/2016) and in the frame of the PRIN 2017 project *Innovative numerical methods for evolutionary partial differential equations and applications*. F.D. was also funded by a *UniTN starting grant* of the University of Trento.

References

References

[1] E. Abbate, A. Iollo, and G. Puppo. An asymptotic-preserving all-speed scheme for fluid dynamics and nonlinear elasticity. *SIAM Journal on Scientific Computing*, 41:A2850–A2879, 2019.

[2] M. Affouf and R.E. Caflisch. A numerical study of riemann problem solutions and stability for a system of viscous conservation laws of mixed type. *SIAM Journal on Applied Mathematics*, 51(3):605–634, 1991.

[3] D.M. Anderson, G.B. McFadden, and A.A. Wheeler. Diffuse-interface methods in fluid mechanics. *Annual review of fluid mechanics*, 30(1):139–165, 1998.

[4] U. Ascher, J. Christiansen, and R.D. Russell. A collocation solver for mixed order systems of boundary value problems. *Mathematics of Computation*, 33(146):659–679, 1979.

[5] U. Ascher, J. Christiansen, and R.D. Russell. Collocation software for boundary-value odes. *ACM Transactions on Mathematical Software (TOMS)*, 7(2):209–222, 1981.

[6] Corentin Audiard and Boris Haspot. Global well-posedness of the euler–korteweg system for small irrotational data. *Communications in Mathematical Physics*, 351(1):201–247, 2017.

[7] G. Bader and U. Ascher. A new basis implementation for a mixed order boundary value ode solver. *SIAM Journal on Scientific and Statistical Computing*, 8(4):483–500, 1987.

[8] S. Benzoni-Gavage. Planar traveling waves in capillary fluids. *Differential and Integral Equations*, 26(3-4):439–485, 2013.

[9] S. Benzoni-Gavage, R. Danchin, and S. Descombes. On the well-posedness for the Euler-Korteweg model in several space dimensions. *Indiana University Mathematics Journal*, 56(4):1499–1580, 2007.

[10] S. Benzoni-Gavage, S. Descombes, D Jamet, and L Mazet. Structure of Korteweg models and stability of diffuse interfaces. *Interfaces and free boundaries*, 7(4):371–414, 2005.

[11] A. Bermúdez, S. Busto, M. Dumbser, J.L. Ferrín, L. Saavedra, and M.E. Vázquez-Cendón. A staggered semi-implicit hybrid FV/FE projection method for weakly compressible flows. *Journal of Computational Physics*, 421:109743, 2020.

[12] W. Boscheri and D.S. Balsara. High order direct arbitrary-lagrangian-eulerian (ale) PNPM schemes with weno adaptive-order reconstruction on unstructured meshes. *Journal of Computational Physics*, 398:108899, 2019.

[13] W. Boscheri, G. Dimarco, R. Loubère, M. Tavelli, and M. H. Vignal. A second order all mach number imex finite volume solver for the three dimensional euler equations. *Journal of Computational Physics*, 415:109486, 2020.

[14] W. Boscheri, M. Dumbser, M. Ioriatti, I. Peshkov, and E. Romenski. A structure-preserving staggered semi-implicit finite volume scheme for continuum mechanics. *Journal of Computational Physics*, 2021:109866, 2010.

[15] D. Bresch, F. Couderc, P. Noble, and J.P. Vila. A generalization of the quantum bohm identity: Hyperbolic cfl condition for euler–korteweg equations. *Comptes Rendus Mathematique*, 354(1):39–43, 2016.

[16] D. Bresch, M. Gisclon, and I. Lacroix-Violet. On navier–stokes–korteweg and euler–korteweg systems: application to quantum fluids models. *Archive for Rational Mechanics and Analysis*, 233(3):975–1025, 2019.

[17] Didier Bresch, Frédéric Couderc, Pascal Noble, and Jean-Paul Vila. New extended formulations of euler-korteweg equations based on a generalization of the quantum bohm identity. *arXiv preprint arXiv:1503.08678*, 2015.

[18] S. Busto, S. Chiocchetti, M. Dumbser, E. Gaburro, and I. Peshkov. High order ADER schemes for continuum mechanics. *Frontiers in Physics*, 8:32, 2020.

[19] S. Busto and M. Dumbser. A new thermodynamically compatible finite volume scheme for magnetohydrodynamics. *SIAM Journal on Numerical Analysis*, 2022. to appear.

[20] S. Busto, M. Dumbser, C. Escalante, S. Gavrilyuk, and N. Favrie. On high order ADER discontinuous Galerkin schemes for first order hyperbolic reformulations of nonlinear dispersive systems. *Journal of Scientific Computing*, 87:48, 2021.

[21] S. Busto, M. Dumbser, S. Gavrilyuk, and K. Ivanova. On thermodynamically compatible finite volume methods and path-conservative ADER discontinuous Galerkin schemes for turbulent shallow water flows. *Journal of Scientific Computing*, 88:28, 2021.

[22] S. Busto, M. Dumbser, I. Peshkov, and E. Romenski. On thermodynamically compatible finite volume schemes for continuum mechanics. *SIAM Journal on Scientific Computing*, 44:A1723–A1751, 2022.

[23] S Busto, JL Ferrín, Eleuterio F Toro, and M Elena Vázquez-Cendón. A projection hybrid high order finite volume/finite element method for incompressible turbulent flows. *Journal of Computational Physics*, 353:169–192, 2018.

[24] S. Busto, E.F. Toro, and E. Vázquez-Cendón. Design and analysis of ADER-type schemes for model advection–diffusion–reaction equations. *Journal of Computational Physics*, 327:553–575, 2016.
[25] P Casal. Capillarité interne en mécanique des millieux continus. *Compt. Rend*, 256(3), 1961.
[26] P Casal. La capillarité interne. *Cahier du groupe français de rhéologie, CNRS VI*, 3:31–37, 1961.
[27] P Casal and H Gouin. A representation of liquid-vapor interfaces by using fluids of second grade. In *Annales de Physique*, volume 13, pages 3–12, 1988.
[28] M.J. Castro, J.M. Gallardo, and C. Parés. High-order finite volume schemes based on reconstruction of states for solving hyperbolic systems with nonconservative products. Applications to shallow-water systems. *Mathematics of Computation*, 75:1103–1134, 2006.
[29] A. Chertock, P. Degond, and J. Neusser. An asymptotic-preserving method for a relaxation of the navier–stokes–korteweg equations. *Journal of Computational Physics*, 335:387–403, 2017.
[30] S. Chiocchetti, I. Peshkov, S. Gavrilyuk, and M. Dumbser. High order ADER schemes and GLM curl cleaning for a first order hyperbolic formulation of compressible flow with surface tension. *Journal of Computational Physics*, 426:109898, 2021.
[31] S. Clain, S. Diot, and R. Loubère. A high-order finite volume method for systems of conservation laws—multi-dimensional optimal order detection (MOOD). *Journal of Computational Physics*, 230(10):4028 – 4050, 2011.
[32] A. Corli, C. Rohde, and V. Schleper. Parabolic approximations of diffusive–dispersive equations. *Journal of Mathematical Analysis and Applications*, 414(2):773–798, 2014.
[33] Constantine M Dafermos. *Hyperbolic conservation laws in continuum physics*, volume 3. Springer.
[34] A. Dedner, F. Kemm, D. Kröner, C.-D. Munz, T. Schnitzer, and M. Wesenberg. Hyperbolic divergence cleaning for the MHD equations. *Journal of Computational Physics*, 175:645–673, 2002.
[35] F. Dhaouadi, N. Favrie, and S. Gavrilyuk. Extended Lagrangian approach for the defocusing nonlinear Schrödinger equation. *Studies in Applied Mathematics*, 142:336–358, 2019.
[36] Firas Dhaouadi. *An augmented lagrangian approach for Euler-Korteweg type equations*. PhD thesis, Université Paul Sabatier-Toulouse III, 2020.
[37] D. Diehl, J. Kremser, D. Kröner, and C. Rohde. Numerical solution of Navier-Stokes-Korteweg systems by Local Discontinuous Galerkin methods in multiple space dimensions. *Applied Mathematics and Computation*, 272:309–335, 10 2016.
[38] G. Dimarco, R. Loubère, V. Michel-Dansac, and M. H. Vignal. Second-order implicit-explicit total variation diminishing schemes for the euler system in the low mach regime. *Journal of Computational Physics*, 372:178 – 201, 2018.
[39] S. Diot, S. Clain, and R. Loubère. Improved detection criteria for the multi-dimensional optimal order detection (MOOD) on unstructured meshes with very high-order polynomials. *Computers and Fluids*, 64:43 – 63, 2012.
[40] S. Diot, R. Loubère, and S. Clain. The MOOD method in the three-dimensional case: Very-high-order finite volume method for hyperbolic systems. *International Journal of Numerical Methods in Fluids*, 73:362–392, 2013.
[41] M. Dumbser. Arbitrary high order PNPM schemes on unstructured meshes for the compressible Navier–Stokes equations. *Computers & Fluids*, 39:60–76, 2010.
[42] M. Dumbser, D. Balsara, E.F. Toro, and C.D. Munz. A unified framework for the construction of one–step finite–volume and discontinuous Galerkin schemes. *Journal of Computational Physics*, 227:8209–8253, 2008.
[43] M. Dumbser, D. S. Balsara, M. Tavelli, and F. Fambri. A divergence-free semi-implicit finite volume scheme for ideal, viscous and resistive magnetohydrodynamics. *International Journal for Numerical Methods in Fluids*, 89:16–42, 2019.
[44] M. Dumbser and D.S. Balsara. High–order unstructured one-step PNPM schemes for the viscous and resistive MHD equations. *CMES - Computer Modeling in Engineering & Sciences*, 54:301–333, 2009.
[45] M. Dumbser, C. Enaux, and E.F. Toro. Finite volume schemes of very high order of accuracy for stiff hyperbolic balance laws. *Journal of Computational Physics*, 227:3971–4001, 2008.
[46] M. Dumbser, F. Fambri, E. Gaburro, and A. Reinarz. On glm curl cleaning for a first order reduction of the ccz4 formulation of the einstein field equations. *Journal of Computational Physics*, 404:109088, 2020.
[47] M. Dumbser and R. Loubère. A simple robust and accurate a posteriori sub-cell finite volume limiter for the discontinuous Galerkin method on unstructured meshes. *Journal of Computational Physics*, 319:163–199, 2016.
[48] M. Dumbser, I. Peshkov, E. Romenski, and O. Zanotti. High order ADER schemes for a unified first order hyperbolic formulation of continuum mechanics: Viscous heat-conducting fluids and elastic solids. *Journal of Computational Physics*, 314:824–862, 2016.
[49] M. Dumbser, I. Peshkov, E. Romenski, and O. Zanotti. High order ADER schemes for a unified first order hyperbolic formulation of Newtonian continuum mechanics coupled with electro–dynamics. *Journal of Computational Physics*, 348:298–342, 2017.
[50] M. Dumbser and O. Zanotti. Very high order PNPM schemes on unstructured meshes for the resistive relativistic MHD equations. *Journal of Computational Physics*, 228:6991–7006, 2009.
[51] M. Dumbser, O. Zanotti, R. Loubère, and S. Diot. A posteriori subcell limiting of the discontinuous Galerkin finite element method for hyperbolic conservation laws. *Journal of Computational Physics*, 278:47–75, 2014.
[52] J Ernest Dunn and James Serrin. On the thermomechanics of interstitial working. In *The Breadth and Depth of Continuum Mechanics*, pages 705–743. Springer, 1986.
[53] M E Eglit. A generalization of the model of an ideal compressible fluid. *J. Appl. Math. Mech.*, 29(2):395–399, 1965.
[54] F. Fambri. A novel structure preserving semi–implicit finite volume method for viscous and resistive magnetohydrodynamics. *International Journal for Numerical Methods in Fluids*, 93:3447–3489, 2021.
[55] N. Favrie and S. Gavrilyuk. A rapid numerical method for solving Serre-Green-Naghdi equations describing long free surface gravity waves. *Nonlinearity*, 30:2718–2736, 2017.

[56] S L Gavrilyuk and S M Shugrin. Media With Equations of State That Depend on derivatives. 37(2):177–189, 1996.
[57] M. Hantke and F. Thein. A general existence result for isothermal two-phase flows with phase transition. *Journal of Hyperbolic Differential Equations*, 16(4):595–637, 2019.
[58] Boris Haspot. Existence of strong solutions for nonisothermal korteweg system. In *Annales Mathématiques Blaise Pascal*, volume 16, pages 431–481, 2009.
[59] T. Hitz, J. Keim, C.D. Munz, and C. Rohde. A parabolic relaxation model for the navier-stokes-korteweg equations. *Journal of Computational Physics*, 421:109714, 2020.
[60] M Jirásek. Jirasek - Nonlocal Theories in Continuum. 44(5), 2004.
[61] A Ya Kipnis, Aleksandr IAkovlevich Kipnis, Boris Efimovich IAvelov, and John Shipley Rowlinson. *Van der Waals and molecular science*. Oxford University Press, 1996.
[62] Diederick Johannes Korteweg. Sur la forme que prennent les équations du mouvements des fluides si l'on tient compte des forces capillaires causées par des variations de densité considérables mais connues et sur la théorie de la capillarité dans l'hypothèse d'une variation continue de la densité. *Archives Néerlandaises des Sciences exactes et naturelles*, 6:1–24, 1901.
[63] M. Lukácová-Medvidóvá, G. Puppo, and A. Thomann. An all Mach number finite volume method for isentropic two-phase flow. *Journal of Numerical Mathematics*, 2022. submitted.
[64] C.D. Munz, P. Omnes, R. Schneider, E. Sonnendrücker, and U. Voss. Divergence Correction Techniques for Maxwell Solvers Based on a Hyperbolic Model. *Journal of Computational Physics*, 161:484–511, 2000.
[65] J. Neusser, C. Rohde, and V. Schleper. Relaxation of the navier–stokes–korteweg equations for compressible two-phase flow with phase transition. *International Journal for Numerical Methods in Fluids*, 79(12):615–639, 2015.
[66] P. Noble and J.P. Vila. Stability theory for difference approximations of some dispersive shallow water equations and application to thin film flows. *arXiv preprint arXiv:1304.3805*, 2013.
[67] C. Parés. Numerical methods for nonconservative hyperbolic systems: a theoretical framework. *SIAM Journal on Numerical Analysis*, 44:300–321, 2006.
[68] I. Peshkov and E. Romenski. A hyperbolic model for viscous Newtonian flows. *Continuum Mechanics and Thermodynamics*, 28:85–104, 2016.
[69] Christian Rohde. A local and low-order navier–stokes–korteweg system. *Nonlinear partial differential equations and hyperbolic wave phenomena*, 526:315–337, 2010.
[70] E.I. Romenski. Hyperbolic systems of thermodynamically compatible conservation laws in continuum mechanics. *Mathematical and computer modelling*, 28(10):115–130, 1998.
[71] John Shipley Rowlinson and Benjamin Widom. *Molecular theory of capillarity*. Courier Corporation, 2013.
[72] F. Thein, E. Romenski, and M. Dumbser. Exact and numerical solutions of the Riemann problem for a conservative model of compressible two-phase flows. *Journal of Scientific Computing*, 2022. submitted.
[73] A. Thomann, G. Puppo, and C. Klingenberg. An all speed second order well-balanced IMEX relaxation scheme for the Euler equations with gravity. *Journal of Computational Physics*, 420:109723, 2020.
[74] V.A. Titarev and E.F. Toro. ADER: Arbitrary high order Godunov approach. *Journal of Scientific Computing*, 17(1-4):609–618, 2002.
[75] V.A. Titarev and E.F. Toro. ADER schemes for three-dimensional nonlinear hyperbolic systems. *Journal of Computational Physics*, 204:715–736, 2005.
[76] E. F. Toro and V. A. Titarev. Derivative Riemann solvers for systems of conservation laws and ADER methods. *Journal of Computational Physics*, 212(1):150–165, 2006.
[77] E.F. Toro. *Riemann Solvers and Numerical Methods for Fluid Dynamics: a Practical Introduction.* Springer, 2009.
[78] Johannes Diederik van der Waals. The thermodynamic theory of capillarity under the hypothesis of a continuous variation of density. *Journal of Statistical Physics*, 20(2):200–244, 1979.
[79] O. Zanotti, F. Fambri, M. Dumbser, and A. Hidalgo. Space-time adaptive ADER discontinuous Galerkin finite element schemes with a posteriori sub-cell finite volume limiting. *Computers and Fluids*, 118:204 – 224, 2015.

Appendix A. Energy conservation

In order to prove energy conservation, it is more convenient to use conserved variables, for which the following notations will be used

$$\mathbf{m} = \rho\mathbf{u}, \quad \varphi = \rho\eta, \quad \omega = \rho w. \tag{A.1}$$

the total energy, expressed in these variables writes

$$\mathcal{E}(\rho, \mathbf{m}, \varphi, \mathbf{p}, \omega, \mathbf{A}, \boldsymbol{\psi}) = \frac{1}{2\rho}|\mathbf{m}|^2 + W(\rho) + \frac{1}{4}cs^2\mathrm{dev}\mathbf{G} : \mathrm{dev}\mathbf{G} + \frac{\gamma}{2}|\mathbf{p}|^2 + \frac{1}{\alpha\rho}(\rho - \varphi/\rho)^2 + \frac{\beta}{2\rho}\omega^2 + \frac{\rho}{2}|\boldsymbol{\psi}|^2 \tag{A.2}$$

We will assume in this part that the cleaning has a rather generic form in order to show how a thermodynamically compatible cleaning is obtained. We will assume in this context that $\nabla \times \mathbf{p}$ and $\nabla \times \boldsymbol{\psi}$, that appear in our evolution equations, are multiplied by two, *a priori* independent, functions of the density, a_p and a_ψ

respectively. Under all the previous notations, it is trivial to verify that HNSK system can be cast into the following compact form

$$\partial_t \rho \ + \nabla \cdot (\rho \mathbf{u}) = 0, \tag{A.3a}$$

$$\partial_t \mathbf{m} + \nabla \cdot \left(\mathbf{u} \otimes \mathbf{m} + \mathcal{E}_\mathbf{p} \otimes \mathbf{p} + \rho \mathbf{A}^T \mathcal{E}_\mathbf{A} \right) + \nabla P = 0, \tag{A.3b}$$

$$\partial_t \mathbf{A} \ + \partial_\mathbf{x} (\mathbf{A} \cdot \mathbf{u}) + \left(\nabla \mathbf{A} - (\nabla \mathbf{A})^T \right) \cdot \mathbf{u} = -\frac{3}{\tau} \left(\det \mathbf{A} \right)^{5/3} \mathbf{A} \mathrm{dev} \mathbf{G}, \tag{A.3c}$$

$$\partial_t \varphi \ + \nabla \cdot (\varphi \mathbf{u}) = \frac{\rho}{\beta} \mathcal{E}_\omega, \tag{A.3d}$$

$$\partial_t \mathbf{p} \ + \partial_\mathbf{x} \mathbf{p} \cdot \mathbf{u} + (\partial_\mathbf{x} \mathbf{u})^T \cdot \mathbf{p} - \nabla(\omega/\rho) + a_p(\rho) \nabla \times \boldsymbol{\psi} = 0, \tag{A.3e}$$

$$\partial_t \omega \ + \nabla \cdot \left(\omega \mathbf{u} - \frac{\gamma}{\beta} \mathbf{p} \right) = -\frac{\rho}{\beta} \mathcal{E}_\varphi, \tag{A.3f}$$

$$\partial_t \boldsymbol{\psi} \ + \partial_\mathbf{x} \boldsymbol{\psi} \cdot \mathbf{u} - a_\psi(\rho) \nabla \times \mathbf{p} = 0. \tag{A.3g}$$

where $P = \rho \mathcal{E}_\rho + \mathbf{m} \cdot \mathcal{E}_\mathbf{m} + \varphi \mathcal{E}_\varphi + \omega \mathcal{E}_\omega$, is the pressure expressed as a function of the total energy. To clarify the convention of differential operators, for any column vector $\mathbf{v}$ and any matrix $\mathbf{A}$ we have

$$\partial_\mathbf{x} \mathbf{v} = \left[\frac{\partial v_i}{\partial x_j} \right]_{ij}, \quad \nabla \mathbf{A} \cdot \mathbf{v} = \left[\frac{\partial A_{ik}}{\partial x_j} u_j \right]_{ik}, \quad \nabla \cdot \mathbf{v} = \frac{\partial v_i}{\partial x_i} \tag{A.4}$$

Now, we multiply every equation by its corresponding entropic variable, that is for every quantity Q we multiply the corresponding evolution equation by $\partial_Q \mathcal{E}$. This allows to write

$$\mathcal{E}_\rho \, \partial_t \rho \quad + \rho \mathcal{E}_\rho \nabla \cdot (\mathbf{u}) + \mathcal{E}_\rho \nabla(\rho) \cdot \mathbf{u} = 0, \tag{A.5a}$$

$$\mathcal{E}_\mathbf{m} \cdot \partial_t \mathbf{m} + \mathcal{E}_\mathbf{m} \cdot \left((\nabla \cdot \mathbf{u}) \, \mathbf{m} + \partial_\mathbf{x} \mathbf{m} \, \mathbf{u} + \nabla \cdot \left(\mathcal{E}_\mathbf{p} \otimes \mathbf{p} - \Sigma \right) \right) + \mathcal{E}_\mathbf{m} \cdot \nabla P = 0, \tag{A.5b}$$

$$\mathcal{E}_\mathbf{A} : \partial_t \mathbf{A} + \mathcal{E}_\mathbf{A} : \nabla \mathbf{A} \mathbf{u} + \mathcal{E}_\mathbf{A} : \mathbf{A} \partial_\mathbf{x} \mathbf{u} = -3 \frac{\det(\mathbf{A})^{5/3}}{\rho \tau c_s^2} \mathcal{E}_\mathbf{A} : \mathcal{E}_\mathbf{A}, \tag{A.5c}$$

$$\mathcal{E}_\varphi \, \partial_t \varphi \quad + \mathcal{E}_\varphi \nabla \varphi \cdot (\mathbf{u}) + \mathcal{E}_\varphi \varphi \nabla \cdot (\mathbf{u}) = \frac{\rho}{\beta} \mathcal{E}_\varphi \mathcal{E}_\omega, \tag{A.5d}$$

$$\mathcal{E}_\omega \, \partial_t \omega \quad + \mathcal{E}_\omega \nabla \omega \cdot \mathbf{u} + \mathcal{E}_\omega \omega \nabla \cdot \mathbf{u} - \frac{1}{\beta} \mathcal{E}_\omega \nabla \cdot \mathcal{E}_\mathbf{p} = -\frac{\rho}{\beta} \mathcal{E}_\omega \mathcal{E}_\varphi, \tag{A.5e}$$

$$\mathcal{E}_\mathbf{p} \cdot \partial_t \mathbf{p} \ + \mathcal{E}_\mathbf{p} \cdot \partial_\mathbf{x} \mathbf{p} \cdot \mathbf{u} + \mathcal{E}_\mathbf{p} \cdot (\partial_\mathbf{x} \mathbf{u})^T \cdot \mathbf{p} - \frac{1}{\beta} \mathcal{E}_\mathbf{p} \cdot \nabla(\mathcal{E}_\omega) + a_p(\rho) \, \mathcal{E}_\mathbf{p} \cdot \nabla \times \boldsymbol{\psi} = 0, \tag{A.5f}$$

$$\mathcal{E}_\boldsymbol{\psi} \cdot \partial_t \boldsymbol{\psi} \ + \mathcal{E}_\boldsymbol{\psi} \cdot \partial_\mathbf{x} \boldsymbol{\psi} \cdot \mathbf{u} - a_\psi(\rho) \, \mathcal{E}_\boldsymbol{\psi} \cdot \nabla \times \mathbf{p} = 0 \tag{A.5g}$$

Summing these equations yields

$$\begin{aligned} \partial_t \mathcal{E} + \Big(& \mathcal{E}_\rho \nabla \rho + (\partial_\mathbf{x} \mathbf{m})^T \, \mathcal{E}_\mathbf{m} + \mathcal{E}_\varphi \nabla \varphi + \mathcal{E}_\omega \nabla \omega + (\partial_\mathbf{x} \mathbf{p})^T \mathcal{E}_\mathbf{p} + (\partial_\mathbf{x} \boldsymbol{\psi})^T \mathcal{E}_\boldsymbol{\psi} + \mathcal{E}_\mathbf{A} : \nabla \mathbf{A} \Big) \cdot \mathbf{u} \\ & + \left(\rho \mathcal{E}_\rho + \mathbf{m} \cdot \mathcal{E}_\mathbf{m} + \mathcal{E}_\varphi \varphi + \mathcal{E}_\omega \omega \right) \nabla \cdot \mathbf{u} - \frac{1}{\beta} (\mathcal{E}_\omega \nabla \cdot \mathcal{E}_\mathbf{p} + \mathcal{E}_\mathbf{p} \cdot \nabla(\mathcal{E}_\omega)) \\ & + \nabla \cdot \left(\mathcal{E}_\mathbf{p} \otimes \mathbf{p} - \Sigma \right) \cdot \mathbf{u} + \nabla P \cdot \mathbf{u} + \mathcal{E}_\mathbf{p} \cdot (\partial_\mathbf{x} \mathbf{u})^T \cdot \mathbf{p} + \mathrm{Tr}(\mathcal{E}_\mathbf{A}^T \mathbf{A} \partial_\mathbf{x} \mathbf{u}) \\ & - a_\psi(\rho) \, \mathcal{E}_\boldsymbol{\psi} \cdot \nabla \times \mathbf{p} + a_p(\rho) \, \mathcal{E}_\mathbf{p} \cdot \nabla \times \boldsymbol{\psi} = -3 \frac{\det(\mathbf{A})^{5/3}}{\rho \tau c_s^2} \mathcal{E}_\mathbf{A} : \mathcal{E}_\mathbf{A} \end{aligned} \tag{A.6a}$$

which leads to

$$\partial_t \mathcal{E} + \nabla \mathcal{E} \cdot \mathbf{u} + (P + \mathcal{E})\, \nabla \cdot \mathbf{u} + \nabla P \cdot \mathbf{u} - \nabla \cdot \left(\frac{1}{\beta} \mathcal{E}_\omega \mathcal{E}_\mathbf{p} \right) + \nabla \cdot \left((\mathcal{E}_\mathbf{p} \otimes \mathbf{p} - \Sigma) \mathbf{u} \right)$$
$$- \mathrm{Tr}\left(\mathcal{E}_\mathbf{p} \otimes \mathbf{p}\, \partial_\mathbf{x} \mathbf{u} \right) + \mathrm{Tr}\left(\Sigma\, \partial_\mathbf{x} \mathbf{u} \right) + \mathcal{E}_\mathbf{p} \cdot (\partial_\mathbf{x} \mathbf{u})^T \cdot \mathbf{p} + \mathrm{Tr}(\mathcal{E}_\mathbf{A}^T \mathbf{A} \partial_\mathbf{x} \mathbf{u})$$
$$- a_\psi(\rho)\, \mathcal{E}_{\boldsymbol{\psi}} \cdot \nabla \times \mathbf{p} + a_p(\rho)\, \mathcal{E}_\mathbf{p} \cdot \nabla \times \boldsymbol{\psi} = -3 \frac{\det(\mathbf{A})^{5/3}}{\rho \tau c_s^2} \mathcal{E}_\mathbf{A} : \mathcal{E}_\mathbf{A} \tag{A.7a}$$

We recall that $\Sigma = -\mathbf{A}^T \mathcal{E}_\mathbf{A} = -\mathcal{E}_\mathbf{A}^T\, \mathbf{A}$. This allows to reduce the last expression to

$$\partial_t \mathcal{E} + \nabla \cdot \left((P + \mathcal{E}) \mathbf{u} + (\mathcal{E}_\mathbf{p} \otimes \mathbf{p} - \Sigma) \mathbf{u} - \frac{1}{\beta} \mathcal{E}_\omega \mathcal{E}_\mathbf{p} \right) - a_\psi(\rho)\, \mathcal{E}_{\boldsymbol{\psi}} \cdot \nabla \times \mathbf{p} + a_p(\rho)\, \mathcal{E}_\mathbf{p} \cdot \nabla \times \boldsymbol{\psi} = -3 \frac{\det(\mathbf{A})^{5/3}}{\rho \tau c_s^2} \mathcal{E}_\mathbf{A} : \mathcal{E}_\mathbf{A} \tag{A.8}$$

The right-hand side of this equation is due to the inherent dissipation of the viscous stresses. In the framework of the GPR model, this dissipative term can be balanced by entropy generation when a non-barotropic equation of state is prescribed [48]. Besides, the are additional terms due to the cleaning procedure which appear on the left hand-side. The GLM curl-cleaning is thus compatible with energy conservation, if and only if these terms can be cast into conservative form. This allows to set a selection criteria for the arbitrary coefficients a_p and a_ψ. Indeed, by replacing $\mathcal{E}_\mathbf{p}$ and $\mathcal{E}_{\boldsymbol{\psi}}$ by their values, these terms become

$$\rho a_\psi(\rho) \boldsymbol{\psi} \cdot \nabla \times \mathbf{p} - \gamma a_p(\rho) \mathbf{p} \cdot \nabla \times \boldsymbol{\psi}. \tag{A.9}$$

One can choose for example $a_\psi(\rho) = \gamma b_c / \rho$ and $a_p(\rho) = b_c$, where b_c is a constant parameter allowing to control the *cleaning speed*. This allows to cast the latter terms in conservative form as follows

$$\gamma b_c (\boldsymbol{\psi} \cdot \nabla \times \mathbf{p} - \mathbf{p} \cdot \nabla \times \boldsymbol{\psi}) = \nabla \cdot (\gamma a_p\, \mathbf{p} \times \boldsymbol{\psi}) \tag{A.10}$$

so that the total energy evolution equation becomes

$$\partial_t \mathcal{E} + \nabla \cdot \left((P + \mathcal{E}) \mathbf{u} + (\mathcal{E}_\mathbf{p} \otimes \mathbf{p} - \Sigma) \mathbf{u} - \frac{1}{\beta} \mathcal{E}_\omega \mathcal{E}_\mathbf{p} + \gamma b_c\, \boldsymbol{\psi} \times \mathbf{p} \right) = -3 \frac{\det(\mathbf{A})^{5/3}}{\rho \tau c_s^2} \mathcal{E}_\mathbf{A} : \mathcal{E}_\mathbf{A} \tag{A.11}$$

This choice of the functions a_c and a_ψ was used throughout this paper.